Xiao, SL., Chen, CJ., Xia, QQ., Liu, Y., Yao, Y., Chen, QY., Hartsfield, M., Brozena, A., Tu, KK., Eichhorn, SJ., Yao, Y., Li, JG., Gan, WT., Shi, SQ., Yang, VW., Lo Ricco, M., Zhu, JY., Burgert, I., Luo, A., ... Hu, LB. (2021). Lightweight, strong, moldable wood via cell wall engineering as a sustainable structural material. *Science*, *374*(6566), 465-471. https://doi.org/10.1126/science.abg9556

Lightweight, Strong, Moldable Wood via Cell Wall Engineering as a Sustainable Structural Material

Shaoliang Xiao[1,*], Chaoji Chen[1,*], Qinqin Xia[1,*], Yu Liu[1*], Yuan Yao[2], Qiongyu Chen[3], Matt Hartsfield[4], Alexandra Brozena[1], Kunkun Tu[5], Stephen J. Eichhorn[6], Yonggang Yao[1], Jianguo Li[1], Wentao Gan[1], Sheldon Q. Shi[7], Vina W. Yang[8], Marco Lo Ricco[8], J-Y Zhu[8], Ingo Burgert[5], Alan Luo[4], Teng Li[3], Liangbing Hu[1,9]†

[1]Department of Materials Science and Engineering, University of Maryland, College Park, Maryland, 20742

[2]Center for Industrial Ecology, Yale School of the Environment, Yale University, New Haven, Connecticut, 06511, USA.

[3]Department of Mechanical Engineering, University of Maryland, College Park, Maryland, 20742, USA.

[4]Department of Materials Science and Engineering, The Ohio State University, Columbus, Ohio, 43210 USA.

[5]Forest Products Laboratory, USDA Forest Service, Madison, Wisconsin, 53726, USA.

[6]Bristol Composites Institute, CAME School of Engineering, University of Bristol, University Walk, Bristol, BS8 1TR, UK.

[7]Department of Mechanical Engineering, University of North Texas, Denton, TX 76203, USA

[8]Wood Materials Science, Institute for Building Materials, ETH Zürich, Zürich 8093, Switzerland.

[9]Center for Materials Innovation, University of Maryland, College Park, Maryland, 20742, USA.

†Email: binghu@umd.edu

*These authors contributed equally to this work.

Keywords: Lightweight structure, Moldable wood, Wrinkling, Wood engineering, Shock process, Environmental sustainability

Abstract

Wood is a sustainable structural material, but it cannot be easily shaped while maintaining its mechanical properties. We report a processing strategy that can shape flat sheets of hardwood into versatile 3D structures based on cell wall engineering. After breaking down wood's lignin component and closing the vessels/fibers by evaporating water, we partially re-swell the wood in a rapid water-shock process that selectively opens the vessels. This forms a distinct wrinkled cell wall structure that allows the material to be folded and molded into desired shapes. The resulting 3D-Molded Wood is six-times stronger than the starting wood and comparable to widely used lightweight materials like aluminum alloys. This approach widens wood's potential as a structural material, with lower environmental impact for buildings and transportation applications.

Shaping and strengthening wood through a rapid "water-shock" process.

The shape of a material can be as important as its intrinsic properties (*1-4*). For example, structural components must be made of materials that can be physically formed to fit specific needs but without sacrificing mechanical strength. Furthermore, materials that are also lightweight are particularly valuable for vehicle-based applications (e.g., cars, trains, and aircraft) (*5*), as weight-saving measures may be the most direct way to improve fuel-efficiency (*6*). For these reasons, polymers and some metals like aluminum (Al) are used for mechanical support, as they feature both low density and facile processability into lightweight structural components of various shapes and sizes by different means such as extrusion, casting, and injection molding (*5, 7*). However, the development of more sustainable materials is needed to mitigate the environmental costs of petrochemical-based plastics and the energy costs of metals (*8-11*).

Wood is one potential candidate for replacing some of these lightweight structural materials, particularly due to its advantage of being a renewable resource (*12, 13*). Wood products can help mitigate climate change by replacing carbon-intensive, fossil-fuel-based materials (*14, 15*), as well as providing extended carbon storage (*16*). Wood is also mechanically strong, lightweight, and potentially low cost. Various approaches have been demonstrated to improve the properties and functionality of wood for a wider range of applications, including by delignification (*17-19*), densification (*20-22*), and other modifications (e.g., thermal treatments (*23*, *24*), organic/inorganic salt impregnation (*25-27*), etc.). However, the formability is generally poor compared to metals and plastics, making processing it into complex shapes difficult.

Different methods of forming wood for shape-specific needs have been explored with varying success. For example, wood can be sculpted into complex three-dimensional (3D) shapes using conventional subtractive manufacturing (e.g., carving, sculpting, turning) (*28, 29*) and conventional carpentry, wherein pieces of wood are joined to make a more complex structure (*30*).

However, these “physical approaches” generally engineer wood at the bulk scale, which does not change the intrinsic microstructure and materials properties, thus failing to simultaneously achieve high mechanical strength and good formability, and limiting the practical applications of wood in advanced engineering fields that require both. In recent years, various bottom-up approaches have also been investigated, in which wood is broken down into its constituent components and then refabricated into desired shapes and uses. For example, defibrillating wood into cellulose nanofibers (CNFs) with exceptional mechanical strength (up to 3 GPa) (*31*) can then be processed into 3D forms via high water content slurries (up to 98 wt.%) (*32*). However, CNFs are expensive, and the energy required for water removal is too intensive for the fabrication of large structures. Alternatively, adding polymers to CNFs can improve the processability by enabling casting or injection molding (*33*). But the high petrochemical polymer content of these CNF composites diminishes their advantage as a sustainable material. Furthermore, such bottom-up approaches come at the sacrifice of wood’s naturally hierarchical and anisotropic structure (i.e., the highly aligned channels/pores and fibers that run along the wood growth direction) where much of the material’s natural strength and functionality derives.

We report a top-down approach that can process wood into various shapes while also substantially increasing its mechanical strength. The principal concept is based on partially delignifying and softening the Natural Wood, then shrinking the vessels and fibers by drying, followed by “shocking” the material in water to selectively open the vessels (Fig. 1A). This rapid water-shock process forms a distinct partially open, wrinkled cell wall structure that provides space for compression as well as the ability to support high strain, allowing the material to be easily folded and molded. The different shapes and structures that can be achieved with this Moldable

Wood can then be set with air drying to remove the remaining water to form the final 3D-Molded Wood product (Fig. 1B).

This cell wall engineering process maintains the intrinsic anisotropic wood structure and enhances the interactions among the wood fibers to further increase the mechanical strength. For example, we demonstrated the fabrication of a honeycomb core material from wood veneers (produced by roll-to-roll rotary cutting) that has a tensile strength of ~300 MPa, similar to Al alloys but with a density of just ~0.75 g/cm^3 and at potentially lower cost (Fig. 1B and 1C). This cell wall engineering approach is applicable to various hardwood species and enabled by the water-shock process that expands the capabilities of wood as a lightweight structural material beyond conventional planar structures to complex 3D designs and components with greater versatility. Manipulating wood's naturally anisotropic structure will improve its potential to be a sustainable and practical alternative for applications that have been traditionally limited to polymers, metals, and polymer composites (Fig. 1C) (*34*).

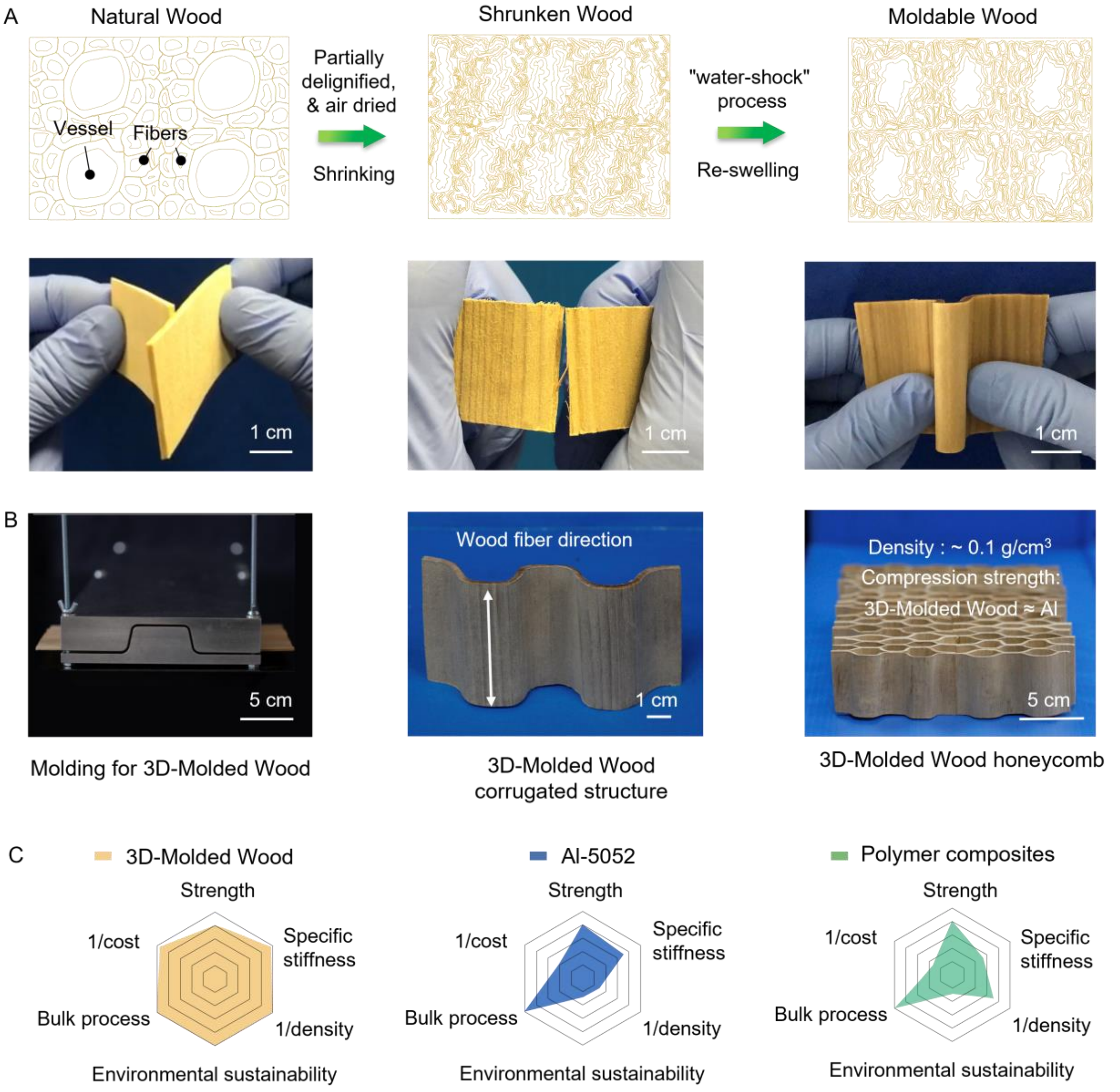

Fig. 1 A wrinkling cell wall engineering strategy through partial delignification combined with a "water-shock" process to make wood stronger and moldable. (A) Schematic illustration of the wood cell wall structures during the fabrication of the Moldable Wood, highlighting the critical role of the water-shock process, which forms wrinkled cell walls. (B) Corrugated and honeycomb 3D-Molded Wood structures made from wood veneers cut parallel to the fiber direction. (C) Radar plots comparing the performance of 3D-Molded Wood, Al-5052 alloy, and

polymer composites (*34*), in which the results are normalized by the maximum value of each characteristic.

We first used a common aqueous-based delignification process (*35*, *36*) to remove ~55% of the lignin and ~67% of the hemicellulose from the lignocellulosic cell walls of basswood (Fig. 1A, figs. S1 to S3). The partial and selective removal of this hydrophobic component results in softening and mild expansion in the wood sample size due to the absorption of water by the remaining cell walls (fig. S1), which feature a higher fraction of hydrophilic cellulose (fig. S2). As a result, the water content of the Partially Delignified Wood is ~300 wt.% water content (fig. S4). We then air dried the Partially Delignified Wood under ambient conditions for ~30 hours to remove water and form the Shrunken Wood intermediate (~12 wt.% water content) (Fig. 1A, fig. S4). Next, we immersed the Shrunken Wood in water for 3 mins in what we termed a water-shock process that partially re-swells the cell walls and leads to some expansion of the sample dimensions in the resulting product, which we call Moldable Wood (~100 wt.% water content, figs. S1, S4, movie S1). While the wet Natural Wood (Fig. 2A) and Shrunken Wood (Fig. 2B) cannot be bent without breaking, the Moldable Wood is highly foldable (Fig. 2C, movie S2). The wood fibers in these samples run parallel to the folding direction. Wood sheets made with this fiber orientation can be scalably produced by rotary cutting, circumventing the size limitations of the length and width of the raw tree material (*37*).

Using scanning electron microscopy (SEM), we examined the microstructures of these wood samples to better understand their process-structure-property relationships. The Natural Wood starting material possesses a 3D hierarchically porous cellular structure with many hollow vessels and fibers (Fig. 2D). These open cells walls become almost completely closed in the Shrunken Wood due to the removal of lignin and water, forming a highly densified structure (Fig.

2E). However, the water-shock treatment that forms the Moldable Wood results in a unique wrinkled cell wall structure in which the vessels are partially open while the fibers are almost completely closed (Fig. 2F). Interestingly, during this treatment we observed the re-opening of the vessels occurs extremely rapidly (3 s) while the morphology of the smaller fibers remains nearly unchanged (movie S3, fig. S5). Such selective opening of the cell wall structure is noteworthy as it may provide two simultaneous effects. The partially open vessels create space within the Moldable Wood that may accommodate both compressive and tensile deformation in an “accordion-like” manner, allowing the material to undergo severe compression and tension while being folded, even up to 180˚ without cracking (Fig. 2C, movie S2). Meanwhile, the densely packed closed fibers may provide mechanical support for enhanced strength.

To further investigate the impact of this wrinkled cell wall structure, we prepared a control in which we air dried the Partially Delignified Wood for just 6 hours and did not apply the water-shock treatment in order to obtain the same water (~100 wt.% water content) and lignocellulosic content as that of the Moldable Wood (fig. S4); The method we used to fabricate this control is similar to that of a previously reported high-strength wood material (*22*). The resulting control did not feature a wrinkled cell wall structure, instead demonstrating a similar open cell microstructure as the Natural Wood but with thinner and more separated cell walls due to the partial removal of the lignin (fig. S6). Additionally, the material could not be bent without breaking (fig. S4), therefore we called it “Non-Moldable Wood.” This control clearly demonstrates the importance of the partially opened, wrinkled cell wall structure in enabling the Moldable Wood’s mechanical flexibility.

We conducted simulations to investigate how the wrinkled cell wall structure enables the release of mechanical stress during folding to prevent the material from breaking. Fiber-scale mechanics modeling shows the strain level in all cell walls of the Moldable Wood is extremely low (with a maximum principal tensile strain of 0.47% and compressive strain of 2.66%) even when the Moldable Wood is subjected to a 60% nominal strain deformation (tensile or compressive; figs. S7 to S8). In contrast, the maximum principal tensile strain in the cell walls of the Non-Moldable Wood is as high as 2.3% under an overall elongation of 12.5%, substantially higher than that in the Moldable Wood (fig. S8). We explain this difference in the mechanical properties of the Moldable and Non-Moldable Wood by their distinct microstructures. Despite both materials undergoing the delignification process, the fibers and vessels are open and only in loose contact in the Non-Moldable Wood, while the cell structures are more closed and in greater contact in the wrinkled cell walls of the Moldable Wood due to the drying/water-shock process. As a result, the Moldable Wood features sufficient hydrogen bonding among the cell walls to resist delamination during folding, while the Non-Moldable Wood readily fractures (fig. S9).

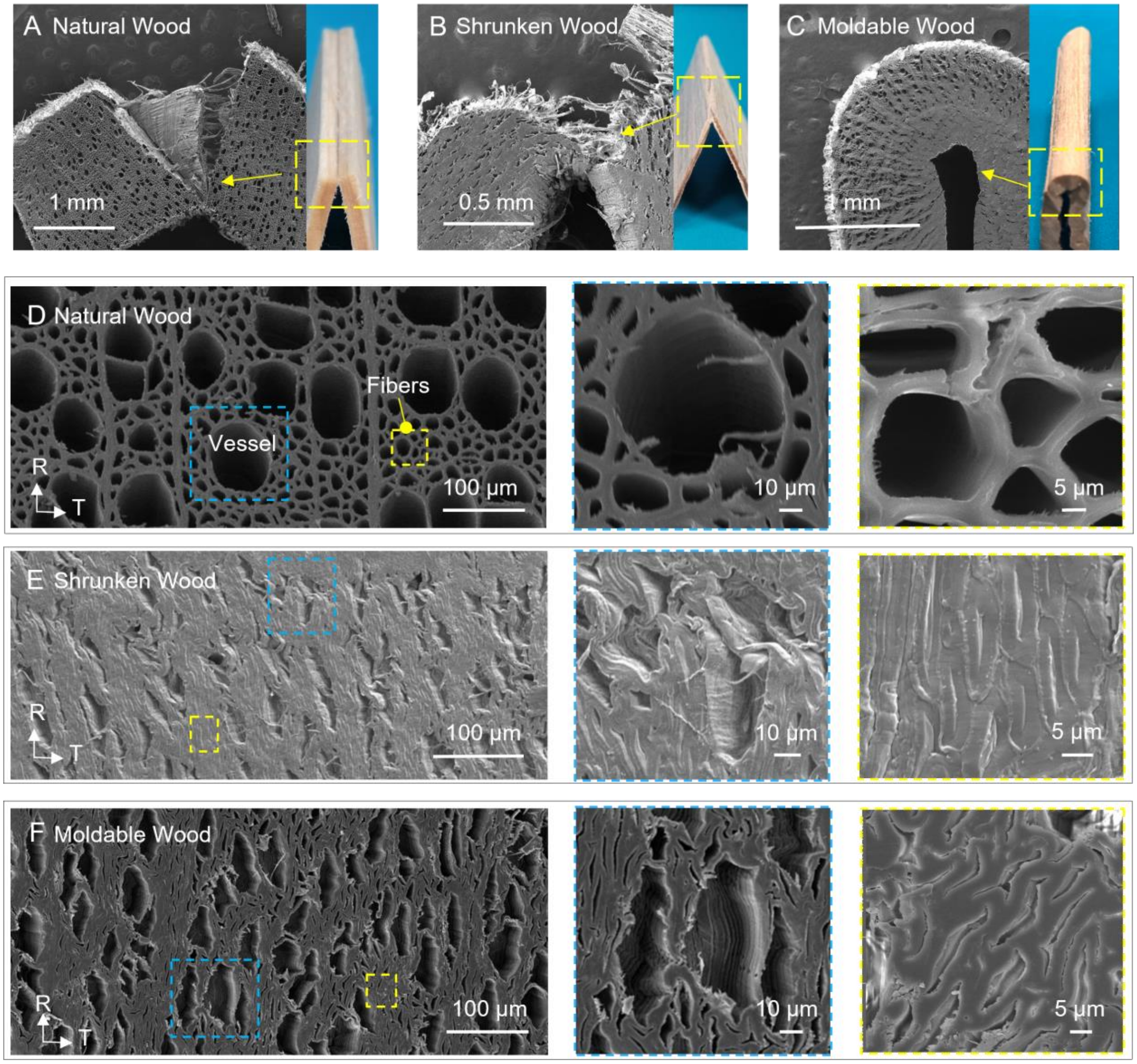

Fig. 2. Microstructures of the Natural Wood, Shrunken Wood, and Moldable Wood. (A–C) Photographs and SEM images demonstrate the (A) Natural Wood and (B) Shrunken Wood undergo deformation and fracture when bent, while (C) the Moldable Wood can be easily folded. (D) SEM images of the Natural Wood, which contains many hollow rigid vessels and fibers. (E) SEM images of the Shrunken Wood, which show the severely shrunken vessels and fibers after water removal. (F) SEM images of the Moldable Wood, which features a unique wrinkled cell wall structure with partially open vessels and almost completely closed fibers.

Using this cell wall engineering method, we can process the Moldable Wood into various shapes by mechanical bending, folding, and twisting. When the targeted structure is achieved, we can then dry the wood to fix its shape. For example, we fabricated zig-zag and corrugated wood structures by repeatedly folding pieces of Moldable Wood and then drying the material to set the rigid forms (Fig. 3A, B). Additionally, we can roll the Moldable Wood (Fig. 3C) and twist it (Fig. 3D, fig. S10, movie S4) like metals and plastics. The outstanding foldability and excellent stability after drying allows us to design and fabricate complex 3D structures, such as star shapes (Fig. 3E). Other shapes include a corrugated structure (25 cm x 12 cm x 0.12 cm) using a homemade die to mold the material (Fig. 3F).

SEM morphology studies reveal the dense and integrated structure of the resulting 3D-Molded Wood. We did not observe any fibers peeling away from the folded corners of these structures, even after 100 folding/unfolding cycles (Fig. 3G). We note the surface finish remains smooth when folded parallel to the wood fiber direction. This excellent surface finish is likely due to the outstanding flexibility of the wood fibers and the hydrogen bonding between them, allowing the fibers to follow the folded shapes during mechanical deformation in a conformal manner (Fig. 3G). In terms of foldability and durability, the Moldable Wood also outperforms Al-5052, a widely used Al alloy for lightweight engineering structures, in which the Moldable Wood can be folded and unfolded 100 times without fracture, while the Al alloy broke after only 3 folding and unfolding cycles (Fig. 3H).

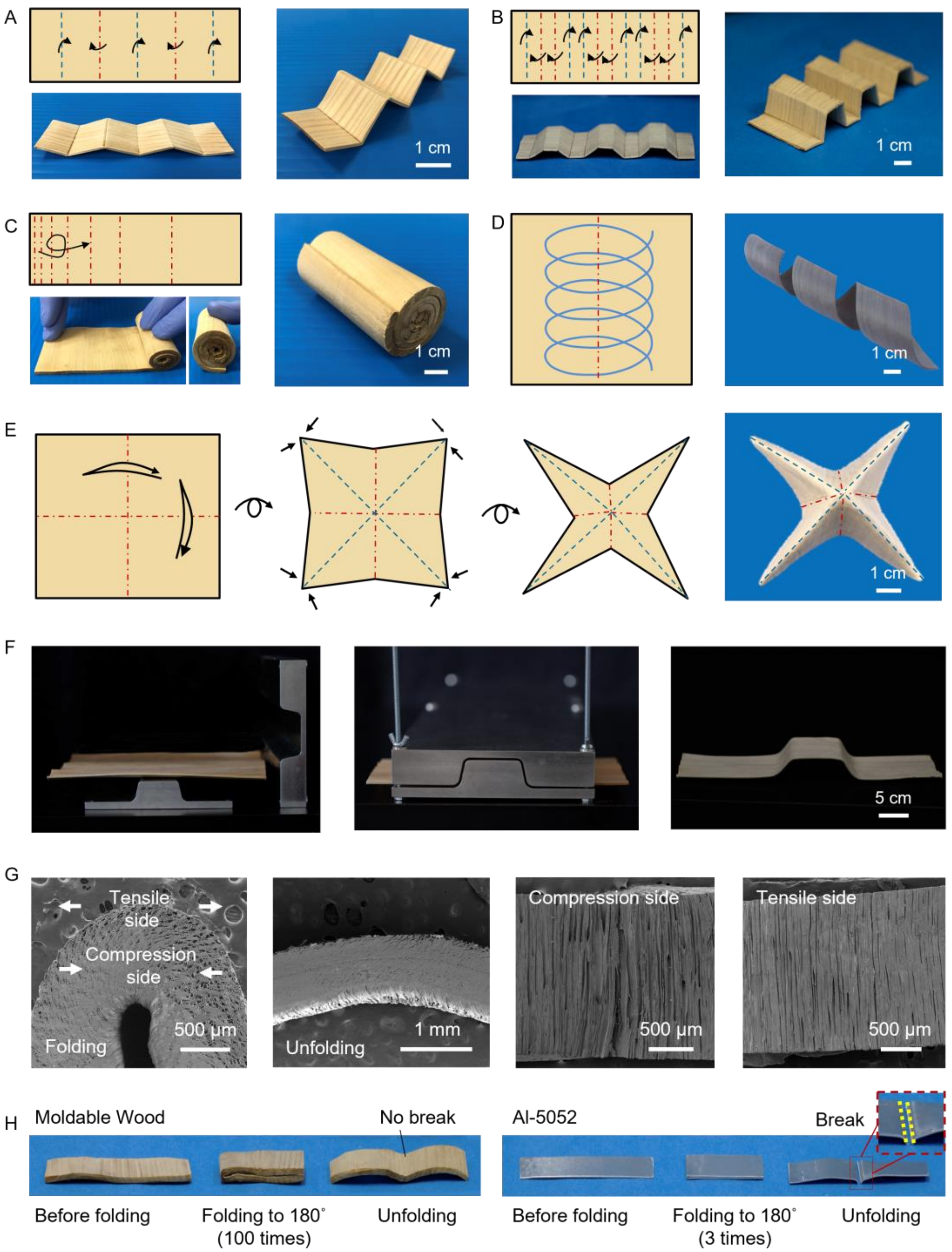

Fig. 3. Fabricating 3D-Molded Wood into various shapes using the cell wall engineering process. Schematics and corresponding photographs of the 3D-Molded Wood featuring (A) zig-zag, (B) corrugated, (C) rolled, (D) helical, and (E) star-shaped structures. (F) The molding process of the 3D-Molded Wood corrugated structure (25 cm x 12 cm x 0.12 cm). (G) SEM images of the

folded and unfolded 3D-Molded Wood, produced after air drying the Moldable Wood after 100 folding/unfolding cycles. We observed no crease in the compression or tensile sides in the resulting 3D-Molded Wood, demonstrating the excellent foldability and durability of the material when folded parallel to the wood fiber direction. (H) Comparison of the Al-5052 alloy and Moldable Wood after undergoing multiple cycles of folding and unfolding. The Moldable Wood remains intact after 100 cycles of folding/unfolding, while the Al alloy breaks after just 3 cycles.

We found the 3D-Molded Wood also has improved mechanical properties for lightweight structural applications, including a tensile strength of ~300 MPa and compressive strength of 60 MPa along the wood fiber direction. These values are 6- and 2-times higher than that of the raw Natural Wood, respectively (fig. S11). The improved mechanical properties of the 3D-Molded Wood are due to its denser structure, which features highly packed intertwined cell walls at the microscale and well-aligned cellulose nanofibrils inside the cell walls at the nanoscale (fig. S12). The 3D-Molded Wood's low density of 0.75 g/cm^3 gives it a high specific tensile strength of 386.8 MPa/(g/cm^3), which is ~5-times greater than that of Al-5052 (84.4 MPa/(g/cm^3); fig. S13). Furthermore, the stiffness of 3D-Molded Wood exceeds that of a range of hardwoods (*38*), softwoods (*38*), and polymers (*39*) (Fig. 4A).

The low density, high mechanical strength, and excellent formability of the 3D-Molded Wood offers broad versatility in designing and manufacturing large, lightweight, load-bearing designs. One example is as honeycomb structure, which is usually made of polymers or metals such as the Al-5052 alloy (*40, 41*). We fabricated 3D-Molded Wood honeycomb structures by molding the material along the wood fiber direction (fig. S14). The 3D-Molded Wood honeycomb unit demonstrates comparable specific compressive strength (51.6 MPa/(g/cm^3)) as the Al-5052 honeycomb unit (46.8 MPa/(g/cm^3)) (Fig. 4B), though the 3D-Molded Wood features the added advantages of potentially being lower cost (table S1) and with potentially enhanced environmental sustainability. To evaluate the compressive and bending properties of the assembled 3D-Molded Wood honeycomb core, we sandwiched the structure between two Al plates (fig. S15). The Al-3D-Molded Wood-Al honeycomb core sandwich demonstrated a compressive strength of 9.1 MPa (Fig. 4C) and specific compressive strength of 91.0 MPa/(g/cm^3), which is higher than that of the Al-5052 honeycomb structure (specific compressive strength of 70.9 MPa/(g/cm^3)) (fig. S16). This sandwich structure was able to support the weight of a 1588 kg car, which corresponds to 1526-times the weight of the 3D-Molded Wood honeycomb core itself (Fig. 4D).

Scaling the manufacturing of corrugated 3D-Molded Wood structures could be accomplished using the mature roll-to-roll manufacturing processes from the wood and pulp industries (Fig. 4E) (*42*). For example, rotary cutting produces large wood sheets, which can be treated by the partial delignification, drying, and water re-swelling steps (fig. S17). All of these processes are common in the wood and pulp industries. Additionally, the 30-hour ambient drying step can be shorted to ~2 mins using hot air (~80 °C) without affecting the material's moldability. Rolling or die forming can then complete the fabrication of 3D-Molded Wood corrugated structures. Additional gluing and assembling steps can create the desired form, a 80 cm x 6 cm x 1.5 cm 3D Molded Wood honeycomb core being one example (Fig. 4F).

In order to replace certain traditional structural materials, like Al alloys (*40*), the long-term durability of 3D-Molded Wood is necessary. Applying a surface coating of polyurethane to the 3D-Molded Wood can help stabilize it against moisture (fig. S18). Moreover, both the uncoated and coated 3D-Molded Wood demonstrates a better anti-fungal property than that of the Natural

Wood (table S2, fig. S19). However, more weathering tests are required to determine the exact types of modifications needed to ensure the long-term durability of the 3D-Molded Wood product. Ensuring uniform production during scale-up and specific performance tests when integrated into various system applications will also help determine the best use for the 3D-Molded Wood.

In addition to its excellent functionality, the 3D-Molded Wood is directly fabricated from a bio-sourced, renewable material (i.e., hardwood species), potentially providing enhanced environmental sustainability (e.g., a lower carbon footprint) compared to traditional metal and polymer-based structural materials. To investigate this potential, we performed a cradle-to-gate Life Cycle Assessment (LCA) to understand the comparative environmental impacts of 3D-Molded Wood and Al alloy (table S3, fig. S20). We calculated the ratio of the environmental impacts per cm^3 of the materials to their tensile strength (MPa) and stiffness (GPa) (tables S4 to S5). Our study included different environmental impact categories, such as those related to ecosystem (acidification, eutrophication, and ecotoxicity), global warming potential, fossil fuel depletion, environmental issues (ozone depletion and smog formation), and human health impacts (including carcinogenic and non-carcinogenic health impacts, and respiratory effects). The 3D-Molded Wood shows substantial reductions (59–99%) across all environmental impact categories, even compared to Al alloy with a high recycled content of 73.9% (Fig. 4G). Such reductions are even larger (74–99% reduction, fig. S21) compared to Al alloy with lower recycled content (35%). Additionally, based on the specific tensile strength measured in this study, 3D-Molded Wood only needs 21–23% of the mass of Al alloy to fulfill the same strength requirements (Equations S3 to S7). LCA results based on the material stiffness, another important mechanical property for a structural material, also show that compared to Al alloy, 3D-Molded Wood has lower environmental impacts in most categories with a few exceptions (figs. S22 to S23). The contribution analysis of the LCA identifies the energy consumption of the wood treatment as the major contributor to the environmental impacts of the 3D-Molded Wood (table S6). However, by reducing the delignification time (table S7; see the Supplemental Materials for more details), the environmental impacts of the 3D-Molded Wood are significantly reduced and lower than Al alloy across all impact categories (figs. S24 to S28).

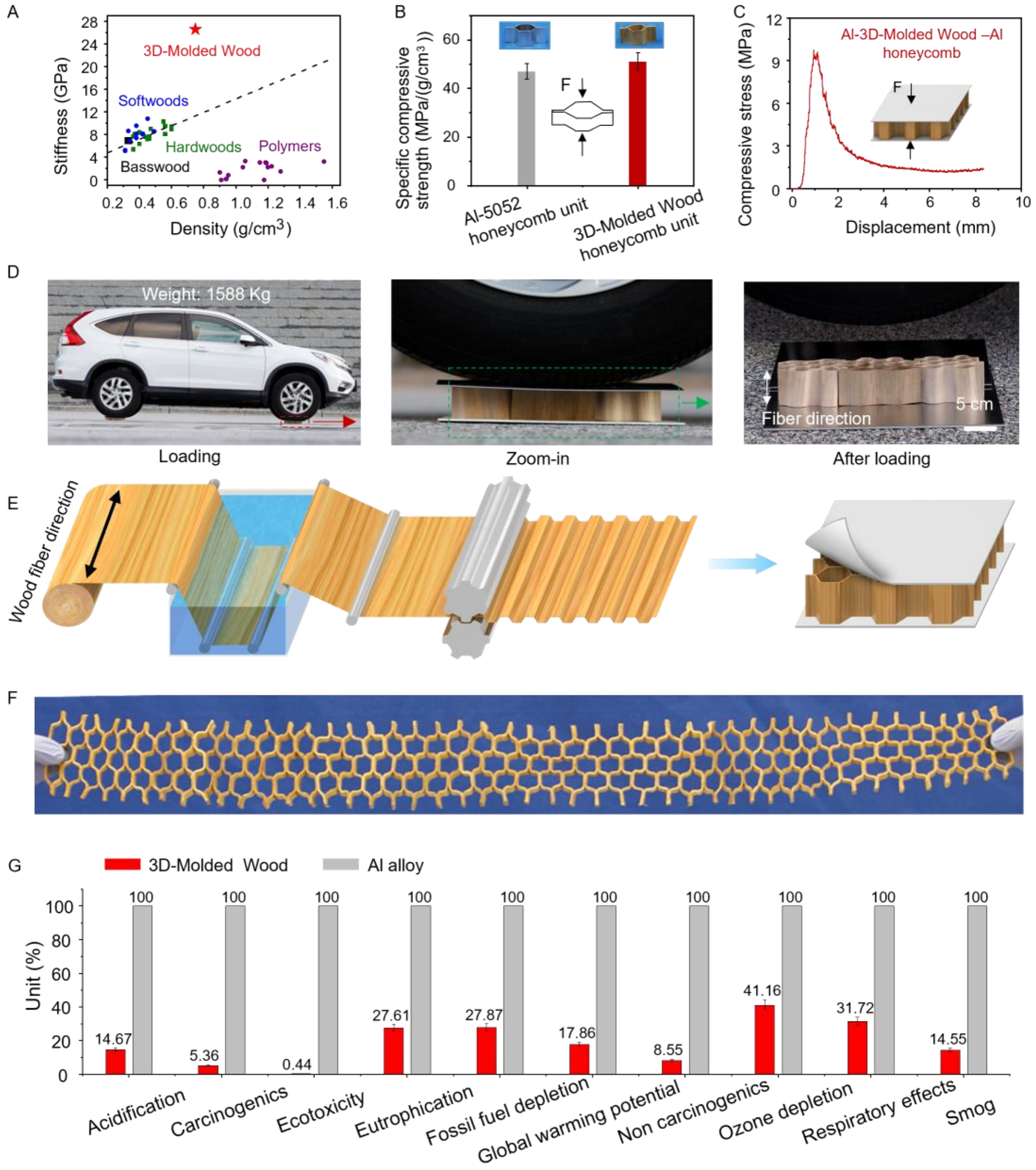

Fig. 4. Mechanical properties and LCA of the 3D-Molded Wood for strong, lightweight structural designs. (A) An Ashby diagram showing the stiffness versus density of 3D-Molded Wood, as well as various wood species *(38)* and polymers (*39*). (B) Comparison of the specific compressive strength of the 3D-Molded Wood and Al-5052 honeycomb units (1.5 cm in height by 2 cm in width and 4.4 cm in length). (C) The compressive stress vs. displacement plot of the Al-3D-Molded Wood-Al honeycomb core sandwich structure. The inset shows the compression test schematic. The 3D-Molded Wood honeycomb core was 1.5 cm in height by 6.5 cm in length and 6 cm in width. (D) Photographs of the sandwich structure supporting the weight of a car, in which the core structure remained intact after loading. (E) Manufacturing process schematic for scaling the fabrication of the 3D-Molded Wood honeycomb core and its potential applications. (F) Photograph of a 3D-Molded Wood honeycomb core, 80 cm in length. (G) The environmental impacts of 3D-Molded Wood and Al alloy (high recycling content of 73.9%) per cm^3/MPa based on the specific tensile strength, normalized to the higher impact material for each environmental impact category.

Conclusion

In this work, we demonstrate how cell wall engineering can render wood foldable and moldable while simultaneously improving its mechanical properties—endowing wood with a structural versatility previously limited to plastics and metals. The 3D-Molded Wood also has several advantages as a sustainable material, with a potentially lower environmental impact compared to Al alloy. 3D-Molded Wood may also enable substantial fuel savings and corresponding environmental benefits when used as a lightweight structural material for vehicles and aircraft. Additionally, wood products have the added benefit, compared to plastics and metals, of large carbon storage capabilities, which is recognized by the Intergovernmental Panel on Climate Change for mitigating global warming (*43*). Furthermore, advances in wood processability and functionality could motivate better forest management practices. We note that in addition to basswood, other hardwood species and of different tree ages and growth locations can be used to fabricate the 3D-Molded Wood by the same treatment, suggesting the universality of this approach to hardwoods and its potential for wide-scale application (figs. S29 to S31). Wood cell wall engineering can substantially expand the versatility of this sustainable and high-performance material, enabling wood as a potential alternative to plastics and metals in structural applications.

References

1. S. Xu *et al.*, Assembly of micro/nanomaterials into complex, three-dimensional architectures by compressive buckling. *Science* **347**, 154-159 (2015).
2. Y. Kim, H. Yuk, R. Zhao, S. A. Chester, X. Zhao, Printing ferromagnetic domains for untethered fast-transforming soft materials. *Nature* **558**, 274-279 (2018).
3. C. Wang, C. Wang, Z. Huang, S. Xu, Materials and structures toward soft electronics. *Adv. Mater.* **30**, 1801368 (2018).
4. Y. Tang *et al.*, Programmable kiri-kirigami metamaterials. *Adv. Mater.* **29**, 1604262 (2017).
5. A. K. Naskar, J. K. Keum, R. G. Boeman, Polymer matrix nanocomposites for automotive structural components. *Nat. Nanotechnol.* **11**, 1026-1030 (2016).
6. A. I. Taub, Automotive materials: technology trends and challenges in the 21st century. *Mrs. Bull.* **31**, 336-343 (2006).
7. K. Zheng, D. J. Politis, L. Wang, J. Lin, A review on forming techniques for manufacturing lightweight complex—shaped aluminium panel components. *Int. J. Lightweight Mater.Manuf.* **1**, 55-80 (2018).
8. X. Liao *et al.*, High strength in combination with high toughness in robust and sustainable polymeric materials. *Science* **366**, 1376-1379 (2019).
9. P. Fratzl, R. Weinkamer, Nature's hierarchical materials. *Prog. Mater. Sci.* **52**, 1263-1334 (2007).
10. Q.-F. Guan *et al.*, Lightweight, tough, and sustainable cellulose nanofiber-derived bulk structural materials with low thermal expansion coefficient. *Sci. Adv.* **6**, eaaz1114 (2020).
11. D. Adam, Aluminium producers promise a cleaner smelting pot (vol 557, pg 280, 2018). *Nature* **558**, 18-18 (2018).
12. C. Chen *et al.*, Structure–property–function relationships of natural and engineered wood. *Nat. Rev. Mater.* **5**, 642-666 (2020).

13. E. Toumpanaki, D. U. Shah, S. J. Eichhorn, Beyond what meets the eye: imaging and imagining wood mechanical–structural properties. *Adv. Mater.* **33**, 2001613 (2021).
14. A. Geng, H. Yang, J. Chen, Y. Hong, Review of carbon storage function of harvested wood products and the potential of wood substitution in greenhouse gas mitigation. *Forest Policy Econ.* **85**, 192-200 (2017).
15. G. Churkina *et al.*, Buildings as a global carbon sink. *Nat. Sustain.* **3**, 269-276 (2020).
16. Y. Pan *et al.*, A large and persistent carbon sink in the world's forests. *Science* **333**, 988-993 (2011).
17. S. Fink, Transparent wood–a new approach in the functional study of wood structure. *Holzforschung* **46,** 403-408 (1992).
18. M. I. Shams, H. Yano, A new method for obtaining high strength phenol formaldehyde resin-impregnated wood composites at low pressing pressure. *J. Trop. For. Sci.* **21**, 175-180 (2009).
19. J. Gierer, Chemistry of delignification. *Wood Science and technology* **19**, 289-312 (1985).
20. R. M. Seborg, M. A. Millett, A. J. Stamm, Heat-stabilized compressed wood (Staypak). (1956).
21. H. Yano, A. Hirose, P. J. Collins, Y. Yazaki, Effects of the removal of matrix substances as a pretreatment in the production of high strength resin impregnated wood based materials. *J. Mater. Sci. Lett.* **20**, 1125-1126 (2001).
22. J. Song *et al.*, Processing bulk natural wood into a high-performance structural material. *Nature* **554**, 224-228 (2018).
23. H. Sivonen, S. L. Maunu, F. Sundholm, S. Jämsä, P. Viitaniemi, Magnetic resonance studies of thermally modified wood. *Holzforschung* **56,** 648-654 (2002).
24. B. F. Tjeerdsma, M. Boonstra, A. Pizzi, P. Tekely, H. Militz, Characterisation of thermally modified wood: molecular reasons for wood performance improvement. *Holz. Roh.Werkst.* **56**, 149-153 (1998).
25. S. Trey, S. Jafarzadeh, M. Johansson, In situ polymerization of polyaniline in wood veneers. *ACS Appl. Mater. Inter.* **4**, 1760-1769 (2012).
26. V. Merk *et al.*, Hybrid wood materials with magnetic anisotropy dictated by the hierarchical cell structure. *ACS Appl. Mater. Inter.* **6**, 9760-9767 (2014).
27. C. Mai, H. Militz, Modification of wood with silicon compounds. Inorganic silicon compounds and sol-gel systems: a review. *Wood. Sci. Technol.* **37**, 339-348 (2004).
28. P. N. Hasluck, Ed., *Manual of Traditional Wood Carving* (Courier Corporation, 1977).
29. M. J. Golden, Ed., *A Laboratory Course in Wood-turning* (Harper & Brothers, 1897).
30. B. Hahn, T.-E. Werner, P. Haller, Experimental and numerical investigations on adhesively bonded tubular connections for moulded wooden tubes. *Constr. Build. Mater.* **229**, 116829 (2019).
31. T. Saito, R. Kuramae, J. Wohlert, L. A. Berglund, A. Isogai, An ultrastrong nanofibrillar biomaterial: the strength of single cellulose nanofibrils revealed via sonication-induced fragmentation. *Biomacromolecules* **14**, 248-253 (2013).
32. A. Walther, J. V. I. Timonen, I. Díez, A. Laukkanen, O. Ikkala, Multifunctional high-performance biofibers based on wet-extrusion of renewable native cellulose nanofibrils. *Adv. Mater.* **23**, 2924-2928 (2011).
33. X. Yang *et al.*, Surface and interface engineering for nanocellulosic advanced materials. *Adv. Mater.* **23**, 2002264 (2021).

34. I. A. Kinloch, J. Suhr, J. Lou, R. J. Young, P. M. Ajayan, Composites with carbon nanotubes and graphene: An outlook. *Science* **362**, 547-553 (2018).
35. C. Chen *et al.*, Highly elastic hydrated cellulosic materials with durable compressibility and tunable conductivity. *ACS Nano* **14**, 16723-16734 (2020).
36. Z. Fang *et al.*, Critical role of degree of polymerization of cellulose in super-strong nanocellulose films. *Matter* **2**, 1000-1014 (2020).
37. A. Dupleix, L. Denaud, L. Bléron, R. Marchal, M. Hughes, The effect of log heating temperature on the peeling process and veneer quality: beech, birch, and spruce case studies. *Eur. J. Wood Wood Prod.* **71**, 163-171 (2013).
38. D. W. Green, J. E. Winandy, D. E. Kretschmann, "Mechanical properties of wood" in *Wood Handbook: Wood as an Engineering Material. Madison, WI: USDA Forest Service, Forest Products Laboratory, 1999. General technical report FPL;(1999) pp. 4.1-4.45*.
39. D. W. A. Rees, Ed., *Mechanics of Optimal Structural Design: Minimum Weight Structures*. (John Wiley & Sons, 2009).
40. T. Bitzer, Ed., *Honeycomb Technology* (Springer Netherlands, 1997).
41. C. Moes, G. Hibbard, Development of melt-stretching technique for manufacturing fully-recyclable thermoplastic honeycombs with tunable cell geometries. *Mater. Design* **141**, 67-80 (2018).
42. M. Peresin *et al.*, Large-scale nanofibrillated cellulose film: an overview on its production, properties, and potential applications. *4th International Conference of Pulping, Papermaking and Biotechnology (ICPPB 2012)*, (2012).
43. B. Netz, O. R. Davidson, P. R. Bosch, R. Dave, L. A. Meyer, *Climate change 2007: Mitigation. Contribution of Working Group III to the Fourth Assessment Report of the Intergovernmental Panel on Climate Change. Summary for Policymakers*. (Intergovernmental Panel on Climate Change (IPCC), Geneva, 2007), pp. 23 pp.

Acknowledgements

The information, data, or work presented herein was funded in part by the Advanced Research Projects Agency - Energy (ARPA-E), U.S. Department of Energy, under award number DE-AR0001025. The views and opinions of the authors expressed herein do not necessarily state or reflect those of the United States Government or any agency thereof. L. Hu also acknowledges support from the University of Maryland A. James Clark School of Engineering. We acknowledge the support of the Maryland Nanocenter, its Surface Analysis Center and AIMLab. We acknowledge Z. Li, S. He, and Z. Lin for their assistance in the car lifting experiment.

Author contributions

S. Xiao, C. Chen, Q. Xia, and Y. Liu contributed equally to this work. L. Hu conceived the concept and supervised the project. L. Hu, S. Xiao and C. Chen designed the experiments. S. Xiao, Q. Xia, and Yu. Liu carried out the wood shaping experiments. S. Xiao, J. Li, YG. Yao, and W. Gan measured the mechanical properties. Q. Xia and Yu. Liu provided characterization via SEM. A. Luo and M. Hartsfield performed the compression and bending tests of the honeycomb structures. T. Li and Q. Chen contributed to the mechanistic modeling of the foldability of the 3D-Molded Wood. K. Tu and I. Burgert contributed to the Raman spectroscopy measurements and analysis. V. Yang performed the anti-fungal measurements. Y. Yao conducted the Life Cycle Assessment. L. Hu, S. Xiao, C. Chen, and Q. Xia analyzed the data of the manuscript. L. Hu, S. Xiao, C. Chen, and A. Brozena wrote the manuscript. All authors commented on the final manuscript.

Data and materials availability:

All data are available in the manuscript or the supplementary materials.

Competing interests:

The authors declare no competing interests.

Supplementary Materials

Materials and Methods
Supplementary Text
Figs. S1 to S31
Tables S1 to S7
Captions for Movies S1 to S4
References (*44*-*66*)

Science
AAAS

Supplementary Materials for

Lightweight, Strong, Moldable Wood via Cell Wall Engineering as a Sustainable Structural Material

This PDF file includes:

Materials and Methods
Supplementary Text
Figs. S1 to S31
Tables S1 to S7
Captions for Movies S1 to S4
References

Other Supplementary Materials for this manuscript include the following:

Movies S1 to S4 (.mp4)

Table of contents

Materials and Methods 5-9

Materials 5

Fabrication process of the 3D-Molded Wood 5

Characterization 6

Water mass ratio of wood samples 6

Moldable Wood foldability modeling 7

Mechanical measurements of the 3D-Molded Wood 7

Compression testing of the Al-3D-Molded Wood-Al honeycomb core sandwich structure 7-8

Stability against moisture measurement 8

Anti-fungal property measurement 8-9

Fig. S1. The scalable fabrication process of Moldable Wood. 10

Fig. S2. Compositional evolution of the wood material before and after the partial delignification. 11

Fig.S3. Raman analysis of cell walls of latewood fibers from the Natural Wood and Partially Delignified Wood. 12

Fig. S4. Schematic demonstrating the fabrication process from Natural Wood to 3D-Molded Wood. 13

Fig. S5. The microstructural change from the Shrunken Wood to Moldable Wood by the water-shock process. 14

Fig. S6. SEM images of the Non-Moldable Wood. 15

Foldability modeling of the Moldable Wood vs. Non-Moldable Wood. 16-20

Fig. S7. Foldability modeling of the Moldable Wood at the vessel scale. 17

Fig. S8. Foldability modeling of the Moldable Wood vs. Non-Moldable Wood at the fiber scale. 20

Fig. S9. SEM images of the Non-Moldable Wood and Moldable Wood in the folding state. 21

Fig. S10. Preparation of the helical 3D-Molded Wood. 22

Fig. S11. The mechanical properties of the Natural Wood and 3D-Molded Wood. 23

Fig. S12. Characterization of the 3D-Molded Wood at the micro/nanoscale. 24

Fig. S13. The mechanical properties of the 3D-Molded Wood and Al-5052. 25

Fig. S14. Preparation of the 3D-Molded Wood honeycomb core material. 26

Table S1. Materials cost of the 3D-Molded Wood and Al-5052 plate. 27

Fig. S15. The fabrication of the Al-3D-Molded Wood-Al honeycomb core sandwich structure. 28

Fig. S16. The compressive strength of the Al-3D-Molded Wood-Al honeycomb core sandwich. 29

Fig. S17. Large-scale fabrication of Moldable Wood veneer using rotary cut natural basswood veneer with dimensions of 100 cm (length) by 30 cm (width) by 0.05 cm (thickness) as the starting material. 30

Fig.S18. The stability of the surface-coated (polyurethane coating) 3D-Molded Wood and 3D-Molded Wood honeycomb core before and after exposure to 95% RH for 2 months. 31

Table S2. The average weight loss (%) of the Natural Wood, coated Natural Wood, 3D-Molded Wood, and coated 3D-Molded Wood after the fungal decay test. 32

Fig.S19. The anti-fungal property of the polyurethane-coated and uncoated wood samples. 32

Methodology for Life Cycle Assessment (LCA). 33–50

Table S3. Inputs and outputs of the 3D-Molded Wood production process presented in this work. 35-36

Fig. S20. The process flow diagram of the LCA system boundary. 39

Table S4. The environmental impacts of 3D-Molded Wood on the basis of mass (per kg) and material properties (per cm^3/MPa for strength and per cm^3/GPa for stiffness). 40

Table S5. The environmental impacts of Al alloy on the basis of mass (per kg) and material properties (per cm^3/MPa for strength and per cm^3/GPa for stiffness). 41

Table S6. Results of the contribution analysis. 42-43

Fig. S21. Environmental impacts per cm^3/MPa based on the specific tensile strength for 3D-Molded Wood prepared from 48-hour delignification treatment in Table S3, normalized to the higher impact material for each environmental impact category (Al alloy in low recycling scenario with 35% recycled content). 43

Fig. S22. Environmental impacts per cm^3/GPa based on the specific stiffness for 3D-Molded Wood prepared from 48-hour delignification treatment in Table S3, normalized to the higher impact material for each environmental impact category (Al alloy in low recycling scenario with 35% recycled content).43-44

Fig. S23. Environmental impacts per cm^3/GPa based on the specific stiffness for 3D-Molded Wood prepared from 48-hour delignification treatment in Table S3, normalized to the higher impact material for each environmental impact category (Al alloy in high recycling scenario with 73.9% recycled content). 44

Fig. S24. Decreasing the delignification (chemical treatment) time from 48 hours to 15 mins without sacrificing the performance. 46

Table S7. Inputs and outputs of the 3D-Molded Wood production process with the shortened wood delignification treatment time (15 mins). 46-48

Fig. S25. Environmental impacts per cm^3/MPa based on the specific tensile strength for 3D-Molded Wood prepared from 15-minute delignification treatment shown in Table S7, normalized to the higher impact material for each environmental impact category (Al alloy in high recycling scenario with 73.9% recycled content). 49

Fig. S26. Environmental impacts per cm^3/GPa based on the specific stiffness for 3D-Molded Wood prepared from 15-minute delignification treatment shown in Table S7, normalized to the higher impact material for each environmental impact category (Al alloy in high recycling scenario with 73.9% recycled content). 50

Fig. S27. Environmental impacts per cm^3/MPa based on the specific tensile strength for 3D-Molded Wood prepared from the 15-minute delignification treatment shown in **Table S7** and coated with PUR, normalized to the higher impact material for each environmental impact category (Al alloy in the high recycling scenario with 73.9% recycled content). 51

Fig. S28. Environmental impacts per cm^3/GPa based on the specific stiffness for 3D-Molded Wood prepared from the 15-minute delignification treatment shown in **Table S7** and coated with PUR, normalized to the higher impact material for each environmental impact category (Al alloy in the high recycling scenario with 73.9% recycled content). 52

Fig. S29. Photographs of 3D-Molded Wood made from various species of hardwoods. 53

Fig. S30. The photographs of 3D-Molded Wood made from basswood with different ages of tree. 54

Fig. S31. The photographs of 3D-Molded Wood made from basswood with different environmental exposures/locations. 55

Movies S1 to S4 56

References 57-60

Materials and Methods

Materials

Basswood (*Tilia americana*), balsa (*Ochroma pyramidale*), walnut (*Juglans regia*), elm (*Ulmus parvifolia*), and paulownia (*Paulownia tomentosa*) were used to fabricate the 3D-Molded Wood (note that balsa, walnut, elm, and paulownia were used to demonstrate the universality of the process). Na_2SO_3 (> 98%, Sigma-Aldrich) and NaOH (> 98%, Sigma-Aldrich) were used for the delignification.

Fabrication process of the 3D-Molded Wood

First, a sheet of Natural Wood (basswood, typical sample dimensions: 3.18 mm x 30 cm x 20 cm, density of 0.43 g/cm^3) was partially delignified by treating with a boiling aqueous solution of 2.5 M NaOH and 0.4 M Na_2SO_3 for 48 hours, followed by immersion in water several times to remove the chemicals. Next, this Partially Delignified Wood (~300 wt.% water content) was air dried at room temperature (25±4 ^oC) and a relative humidity (RH) of 45–60% for 30 hours to form the Shrunken Wood intermediate (~8–12 wt.% water content), which was then immersed in water for 3 mins (i.e., the "water-shock" process) to form the Moldable Wood (~100 wt.% water content). Finally, the 3D-Molded Wood (density of 0.75 g/cm^3, ~8–12 wt.% water content) was achieved by shaping the Moldable Wood into the desired structure and removing water from the material by air-drying at room temperature for 30 hours.

To investigate the impact of the wrinkled cell wall structure of the Moldable Wood, we prepared a Non-Moldable Wood control by air drying the Partially Delignified Wood for ~6 hours and without applying the water-shock treatment. As a result, the Non-Moldable Wood featured the same water and compositional content as the Moldable Wood sample (Fig. S4).

Characterization

The microstructures of the wood samples were observed by a Hitachi SU-70 SEM. Optical microscopy was performed using an OLYMPUS BX51M. Fourier transform infrared spectroscopy (FTIR) was recorded on a Thermo Nicolet Nexus 6700 spectrometer over the range of 4000–600 cm^{-1} to determine the functional groups of the wood samples. The chemical composition of the Natural Wood and Moldable Wood was measured using a two-step sulfuric acid hydrolysis method, as described previously (*44*). Small-angle X-ray scattering (SAXS) patterns of the 3D-Molded Wood were collected using a Rigaku MicroMax 007HF (operating voltage of 40 kV, current of 30 mA, CuKα, $\lambda = 0.1541$ nm).

Water mass ratio of the wood samples

The water content of the wood samples was determined based on the mass of the oven-dried wood. The water mass ratio of the wood samples was calculated according to the following formula:

$$Water\ mass\ ratio\ (\%) = (W_1 - W_0)/W_0 \times 100 \qquad \text{(Equation S1)}$$

where W_1 and W_0 are the weights of the wood sample before and after oven drying for 6 hours at 103 °C, respectively.

According to the above equation, the water content of all wood samples was determined to be ~8–12 wt.% for Natural Wood, ~300 wt.% for the Partially Delignified Wood, ~100 wt.% for the Non-Moldable Wood, ~8–12 wt.% for the Shrunken Wood, ~100 wt.% for the Moldable Wood, and ~8–12 wt.% for the 3D-Molded Wood.

Moldable Wood foldability modeling

The two-scale mechanics modeling was performed using the finite element code ABAQUS 2019. All simulation models assumed a plane strain condition, which was justified by the sample geometry and material structure of the Moldable Wood. Based on the SEM images of the wood structure, the vessels in the Moldable Wood were modeled by an array of circular holes with a diameter of 50 μm in a triangular lattice with an inter-vessel distance of 50 μm. The cell wall structure was modeled as a honeycomb network with a 2 μm cell wall thickness and a 20 μm side length of a single hexagon. The Moldable Wood was assumed to be a linear elastic material with a Poisson's ratio of 0.346 in the modeling plane (*38*).

Mechanical measurements of the 3D-Molded Wood

The tensile and compressive properties of the samples were measured using an Instron 5565 universal tester with a 30 kN load cell at room temperature (25±4 ^{o}C) and 45–60% RH. The dimensions of the tensile samples were approximately 100 mm x 5 mm x 1 mm. The samples were clamped at both ends and stretched along the wood fiber direction with a constant test speed of 5 mm min^{-1}. The dimensions of the compressive samples were approximately 10 mm (length) x 5 mm (width) x 5 mm (thickness), and the samples were compressed along the wood fiber direction at a speed of 1 mm min^{-1}.

Compression testing of the Al-3D-Molded Wood-Al honeycomb core sandwich structure

The compression tests for the Al-3D-Molded Wood-Al honeycomb core sandwich structures were performed on an MTS Criterion Model 43 with a 30 kN load cell at room temperature (25±4 ^{o}C) and 45–60% RH. Test samples were comprised of a 3D-Molded Wood honeycomb core sandwiched between two Al-5052 sheets (1 mm thick). The 3D-Molded Wood honeycomb core by itself was 65 mm x 60 mm x 15 mm, with a cell width of 10 mm; the assembled structure was 82 mm x 75 mm x 17 mm.

Stability against moisture measurement

The stability test against moisture was performed in a humidity chamber (LHS-150HC-II). The humidity chamber was set at 20 °C, 95% RH. We used a painting method (widely used in the wood industry) to coat the 3D-Molded Wood (60 mm x 40 mm x 4 mm) and 3D-Molded Honeycomb core (61 mm x 53 mm x 10 mm) with a thin layer of oil-based paint (Polyurethane, Minwax). After the paint was completely dry, these two samples were placed in the humidity chamber for 2 months. The dimensions and weight of the samples after various intervals in the humidity chamber were recorded. In addition, we tested the mechanical strength of the coated 3D-Molded Wood immediately after exposure to 95% RH for 2 months.

Anti-fungal property measurement

We used the American Wood Preserver's Association E-10-12 (AWPA 2014) Standard to test the biodegradation of our wood samples by decay fungi. Two wood decay fungi, brown rot fungus *Postia placenta* and white rot fungus *Phanerochaete chrysosporium*, were used to test the degradation susceptibility of the four types of wood samples. Isolates of two decay fungi, *P. placenta* (Fr.) M.Lars and Lomb. (MAD 698) and *P. chrysosporium* (F1767), were grown and maintained on 2% malt extract agar (Difco, Detroit, Michigan) in petri dishes (15 mm x 100 mm). Fungal inoculum was incubated at 27 ^{o}C, 70% RH room for three weeks. Four types of wood specimens were studied, including Natural Wood, 3D-Molded Wood, and coated Natural Wood and coated 3D-Molded Wood, which were coated with an oil-based paint (Polyurethane, Minwax). All specimens were 2 cm x 3 cm in size and conditioned in an incubator for two weeks. After the weights were measured, the specimens were laid on agar plates containing confluent fungal growth. The plates were then incubated according to the AWPA 2014 Standard with modifications. No overlaying grids were used for the petri dishes. The petri dishes were incubated at 27 °C, 70% RH to promote fungal growth over the specimens. Evaluations of growth were observed on day 0 and weeks 4, 8, and 12. Photographs were taken at each time point. To determine the weight loss of the samples, the wood specimens were harvested on week 12; the fungal mycelia were brushed off, dried at 40°C for 72 hours and reconditioned in an incubator at 27 °C, 70% RH for two weeks to obtain the final wood specimen weights. The weight loss by decay fungi was determined by subtracting the reconditioned harvest weights from the original conditioned weights. Percentage weight loss was calculated.

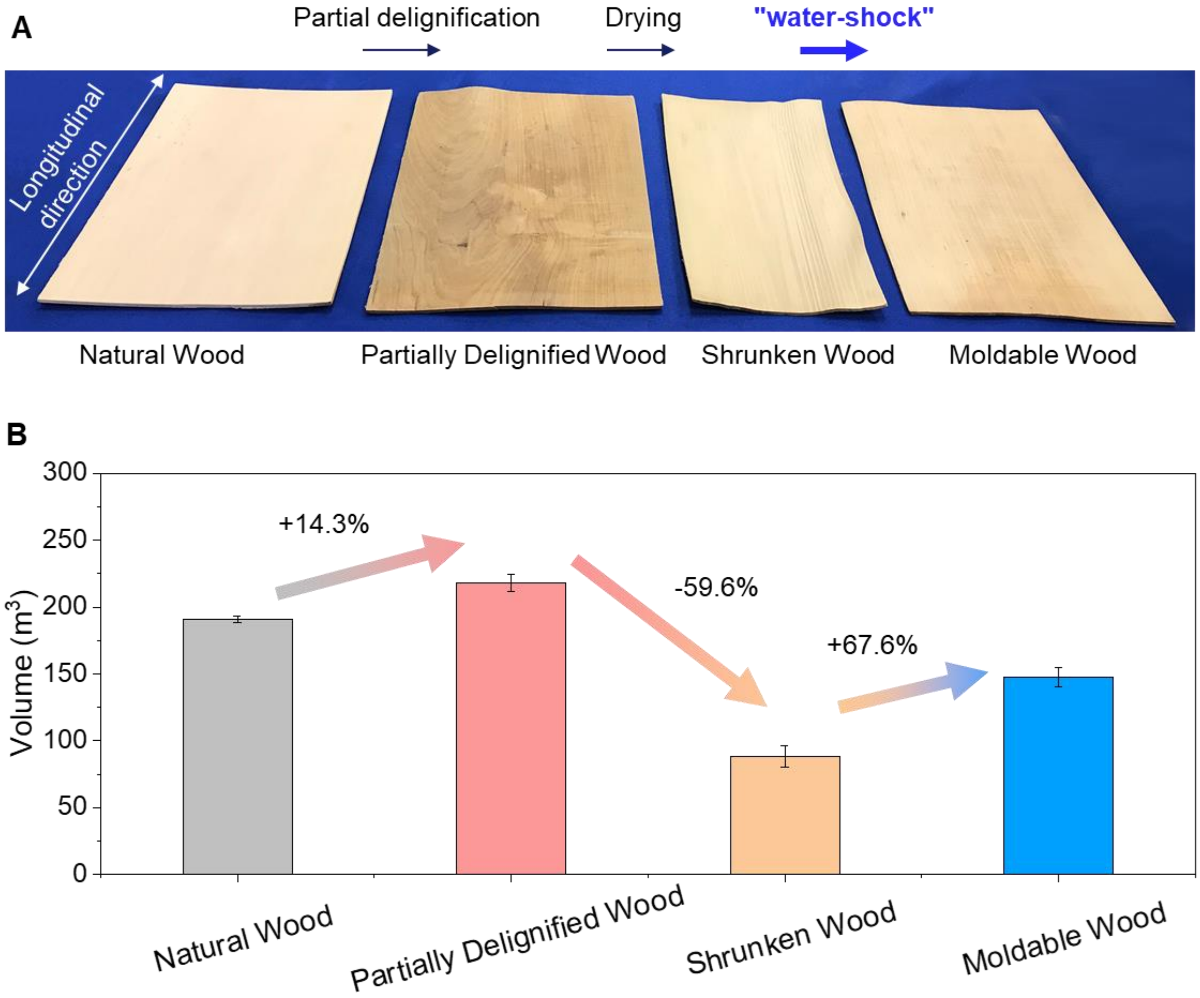

Fig. S1. The scalable fabrication process of Moldable Wood. (A) Photographs and (B) the volume evolution of the Natural Wood (basswood), Partially Delignified Wood, Shrunken Wood, and Moldable Wood.

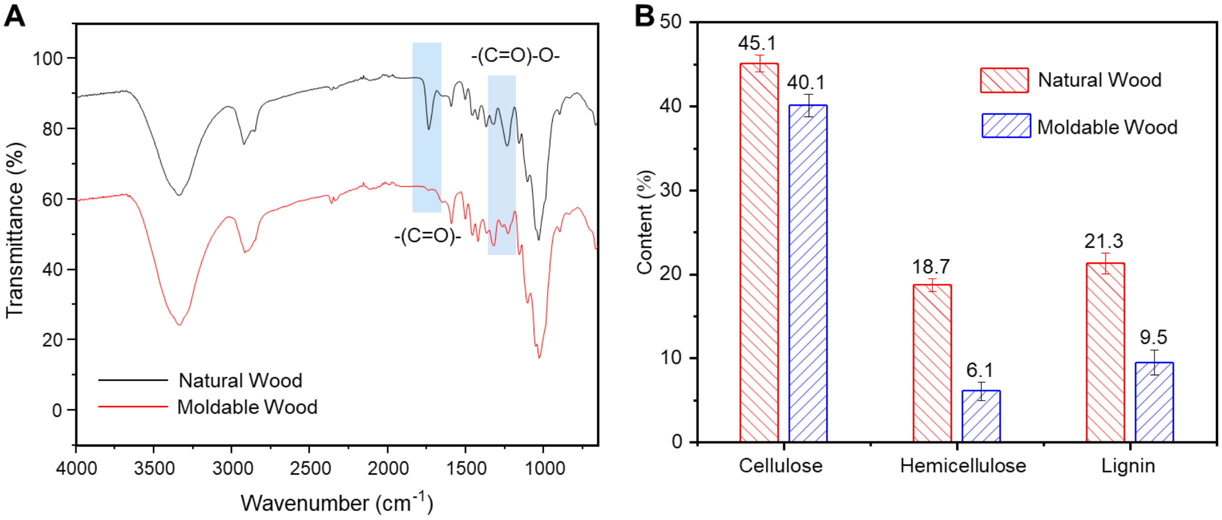

Fig. S2. Compositional evolution of the wood material before and after partial delignification. (A) FTIR of the Natural Wood (basswood) and Moldable Wood. The Moldable Wood features a decrease in the peak intensities at 1735 cm^{-1} and 1230 cm^{-1}, which respectively correspond to the carboxyl groups of hemicellulose and the ester linkage of the carboxyl groups of lignin and/or hemicellulose, showing the partial removal of the lignin and hemicellulose by the NaOH/Na_2SO_3 treatment. (B) Evolution of the cellulose, hemicellulose, and lignin content from the Natural Wood to Moldable Wood. The results show that cellulose, hemicellulose, and lignin are partially removed by the chemical treatment.

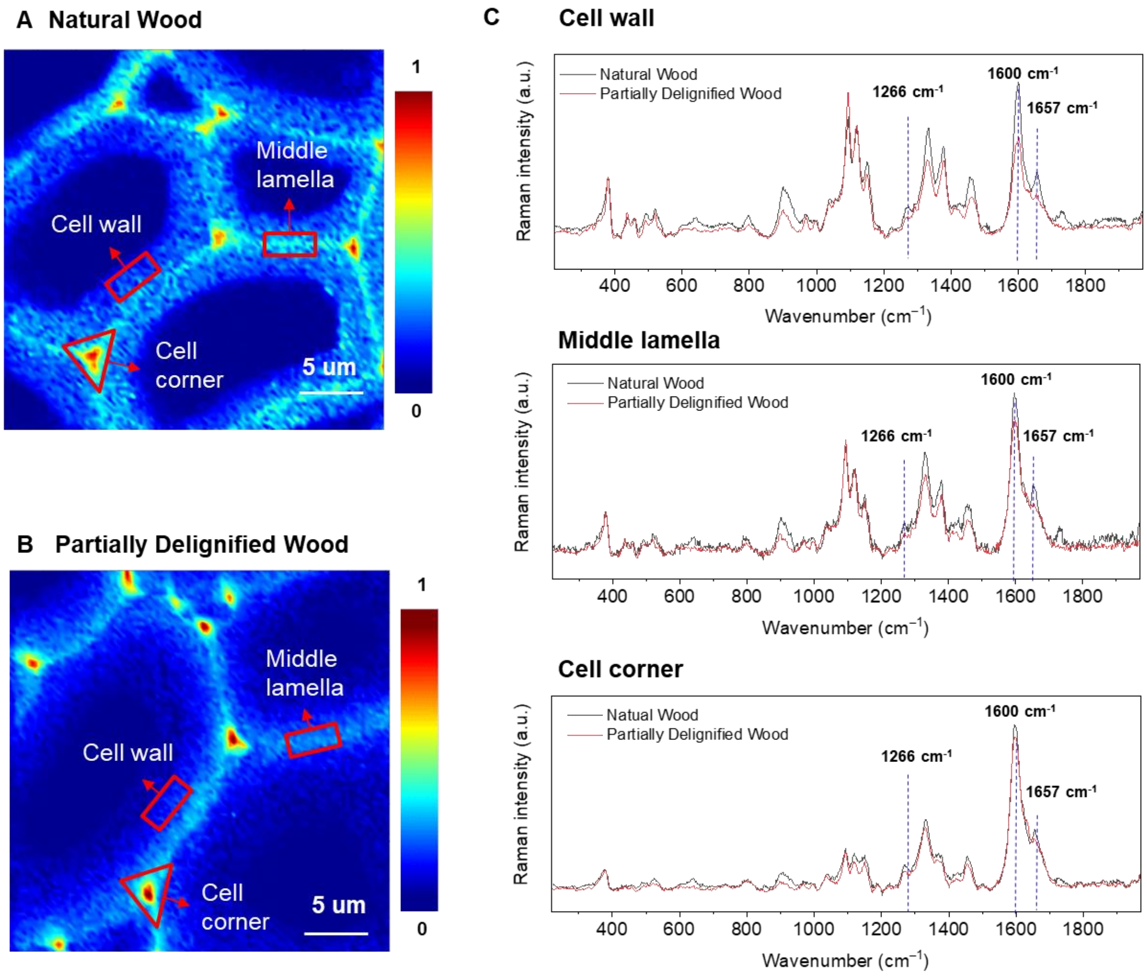

Fig. S3 Raman analysis of the cell walls of latewood fibers from the Natural Wood and Partially Delignified Wood. (A, B) Raman images of the (A) Natural Wood and (B) Partially Delignified Wood cells. (C) The corresponding Raman spectra at different locations of the Natural Wood and Partially Delignified Wood, including the secondary cell walls, middle lamellae, and cell corners (as shown in (A) and (B)). The characteristic bands of lignin occur at 1266 cm^{-1}, 1600 cm^{-1}, and 1657 cm^{-1}. The spectra show that some fraction of the lignin of the fibers has been removed by the delignification process. The degree of delignification is highest in the secondary cell walls, less in the middle lamellae, and the lowest in the cell corners. The Raman spectroscopy results indicate that the lignin in the cell walls is partially and selectively removed by the chemical treatment.

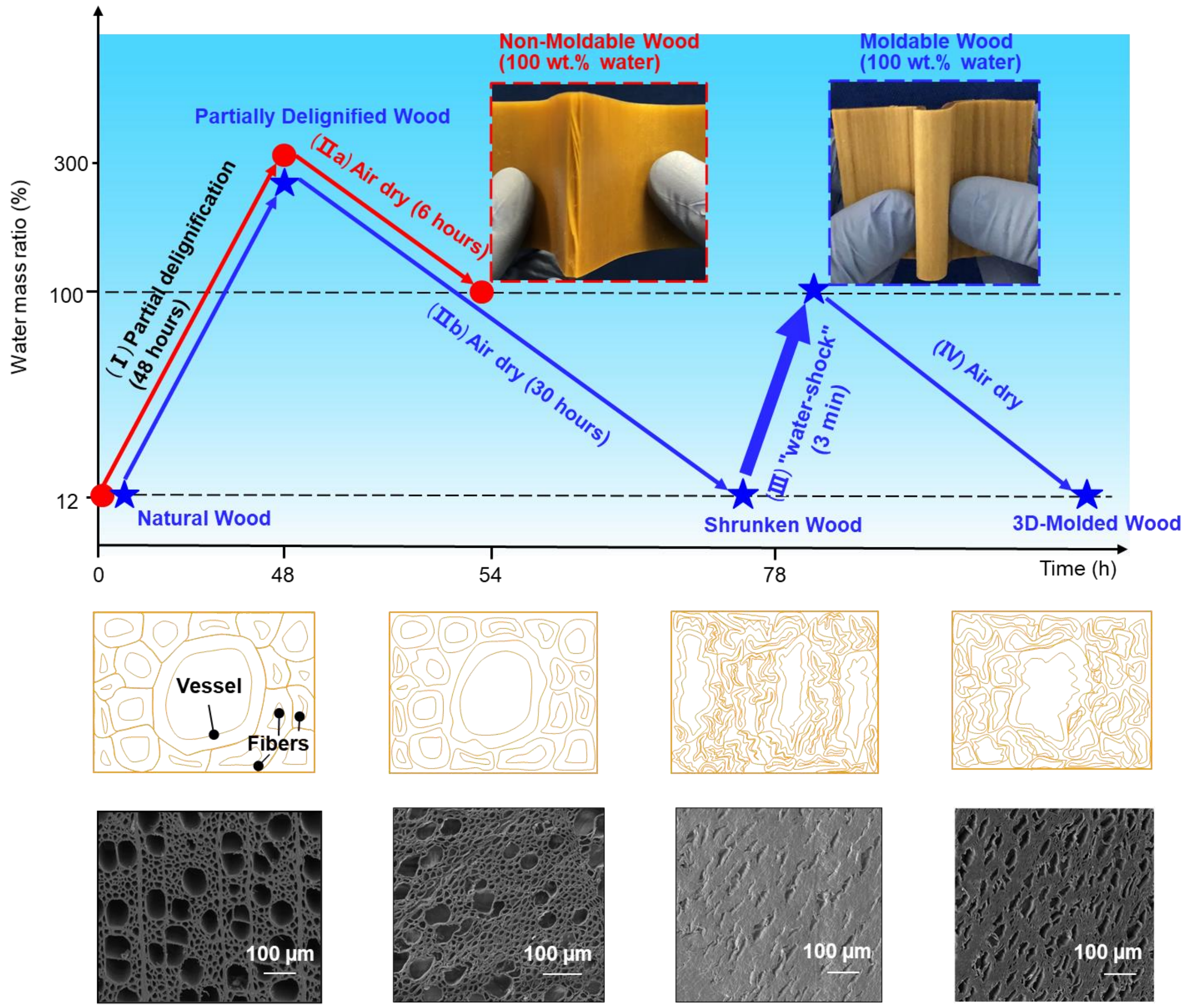

(Ⅰ) Natural Wood
(8 - 12 wt.% water)

(Ⅱ) Non-Moldable
Wood (100 wt.% water)

(Ⅲ) Shrunken Wood
(8 - 12 wt.% water)

(Ⅳ) Moldable Wood
(100 wt.% water)

Fig. S4. Schematic demonstrating the fabrication process from Natural Wood to 3D-Molded Wood. To fabricate 3D-Molded Wood, Natural Wood is first delignified to partially remove the brittle lignin component of the wood cell walls, forming the Partially Delignified Wood, which is then air dried over a period of 30 hours, causing the cell walls to shrink, closing both the large and small channels (i.e., vessels and fibers, respectively) to obtain the Shrunken Wood intermediate. The Shrunken Wood is then “shocked” by briefly soaking (3 mins) the wood in water to obtain the Moldable Wood. The Moldable Wood has a unique cell wall structure in which the vessels and fibers become “wrinkled” upon swelling. The Moldable Wood can be folded and molded into arbitrary shapes that can then be locked in place by drying the material for a final time to obtain the 3D-Molded Wood final product. As a control, we delignified Natural Wood using the same procedure, but then air-dried the material for just 6 hours to reach a ~ 100 wt.% water content – the same as that of the Moldable Wood. However, this control (i.e., Non-Moldable Wood) is not as flexible; instead breaking when it is bent due to the lack of a wrinkled cell wall structure.

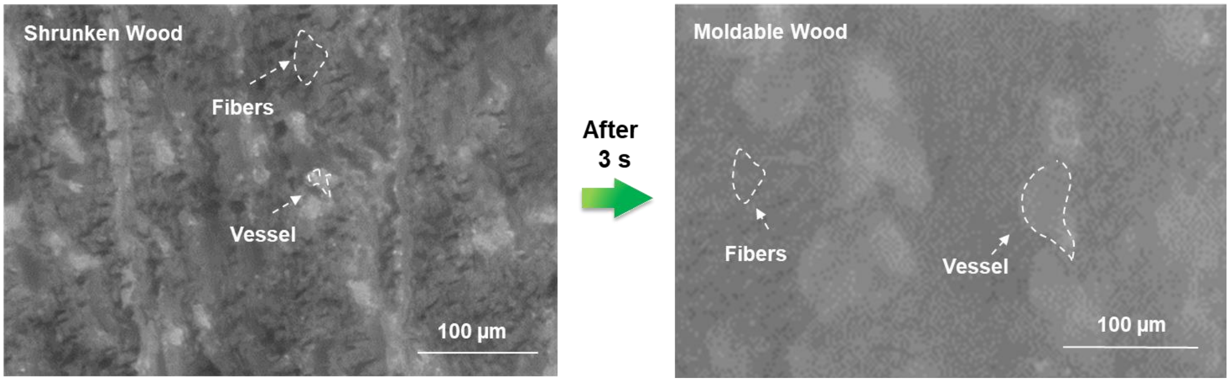

Fig. S5. The microstructural change from the Shrunken Wood to Moldable Wood by the water-shock process. Optical microscopy images of the Shrunken Wood in the dry state (left) vs. the Moldable Wood in the wet state (right) show the material's structure changes rapidly (3 s), in which the wood vessels selectively open upon immersion in water.

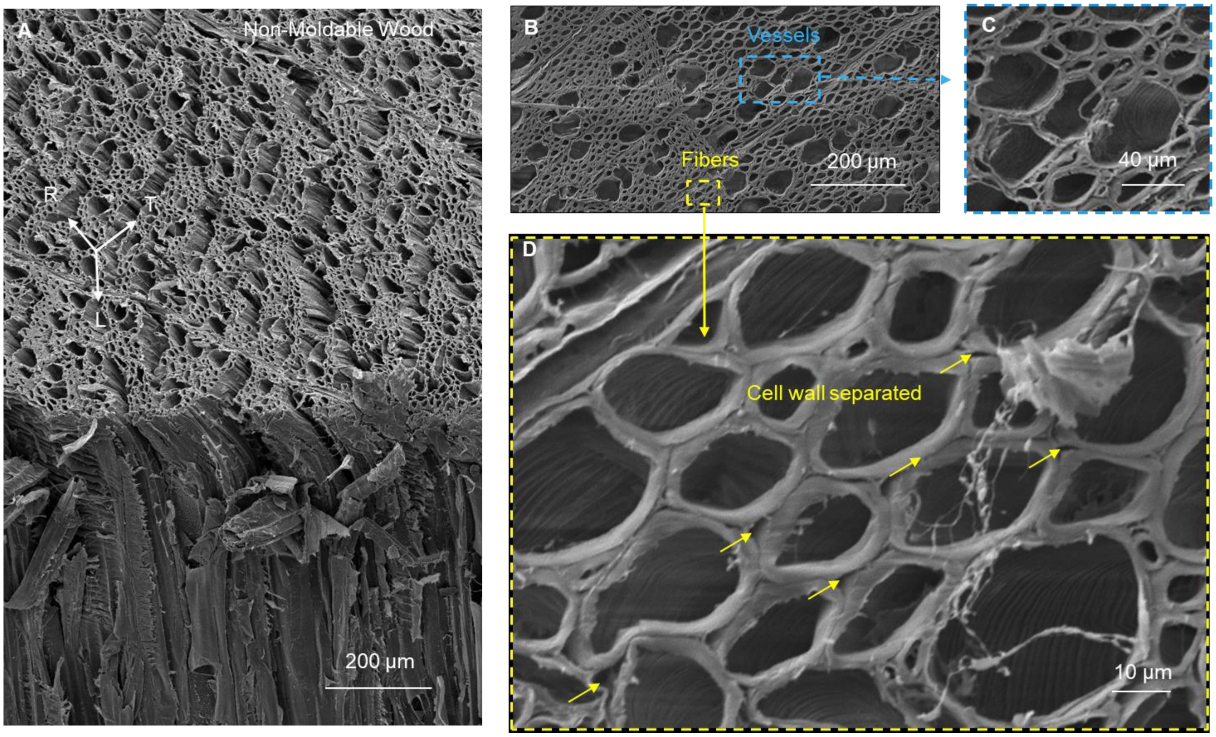

Fig. S6. SEM images of the Non-Moldable Wood. (A) SEM image of the Non-Moldable Wood, in which the open structures of the fibers and vessels were retained after the partial delignification process. (B) Cross-sectional SEM image of the Non-Moldable Wood, showing a top view of the fibers and vessels. (C, D) Magnified cross-sectional SEM image of the (C) vessels and (D) fibers, showing the separated cell walls.

Foldability modeling of the Moldable Wood vs. Non-Moldable Wood.

We performed two-scale hierarchical mechanics modeling to reveal the strain mitigation mechanism of the Moldable Wood under severe folding. The first scale was at the vessel level. As illustrated in the top two panels in Fig. S7A, the modeling at this scale featured the Moldable Wood with an array of circular holes (i.e., vessels). The second scale was at the fiber level. As illustrated in the bottom two panels in Fig. S7A, the modeling at this scale focused on the hollow nature of the fiber structures in the region between neighboring vessels. As detailed below, the vessels and fibers can effectively reduce the strain level in a synergistic fashion when the Moldable Wood is subjected to severe folding. Fig. S7B and C show the model of the Moldable Wood (with vessels) in its flat state and after 180˚ folding about the midpoint of the material. In the contour plot, the outer part of the severely folded region is under tension and the inner part is under compression, with a neutral area (zero strain) near the middle plane along the thickness direction of the Moldable Wood. It has been previously shown that circular holes (e.g., the distributed vessels in Moldable Wood) can effectively reduce the strain level in a material subject to large deformation (*45*). As further shown in Fig. S7D, the patterned vessel array also appears to provide a similar strain mitigation effect for the Moldable Wood under all folding angles ranging from 0˚ to 180˚. As shown in the modeling at the fiber scale (Fig. S8), the hollow cell wall structure in the regions between neighboring vessels of the Moldable Wood can further reduce the strain level in the cell walls, even if the Moldable Wood is subject to severe folding.

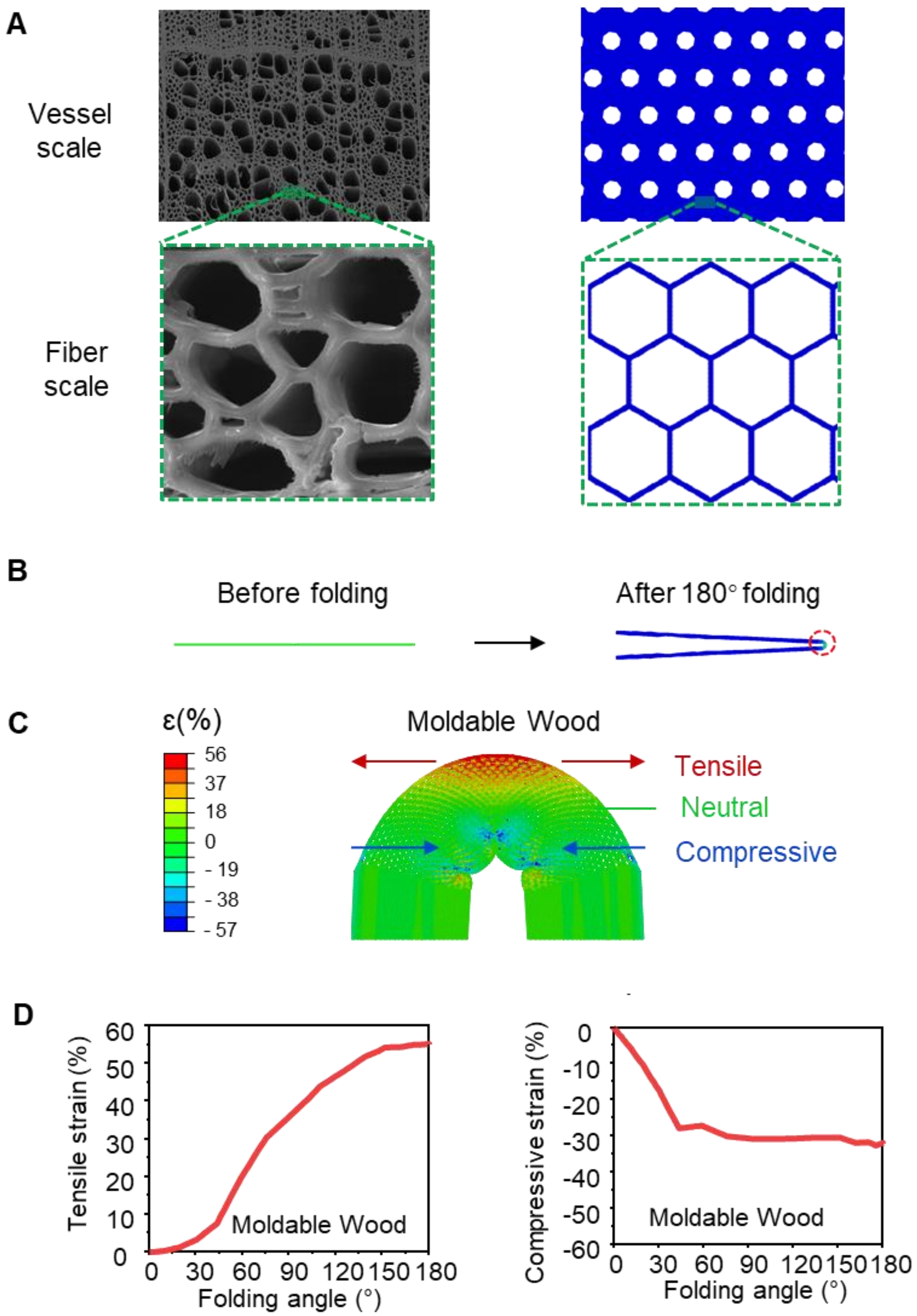

Fig. S7. Foldability modeling of the Moldable Wood at the vessel scale. (A) The hierarchical structure of the Moldable Wood with features at two scales: a larger scale with vessels distributed in an array and a smaller scale with hollow fibers. Both SEM images at the two scales of the hierarchical structure and the corresponding simulation models are shown. (B) Vessel scale modeling of a piece of Moldable Wood under 180˚ folding. (C) Contour plot of the strain in the severely folded region of the Moldable Wood (corresponding to the region highlighted by the dashed circle in (B)). (D) The maximum tensile (left) and compressive (right) strain in the severely folded region of the Moldable Wood as a function of the folding angle from 0˚ to 180˚.

Fig. S8A plots the finite element modeling results at the fiber scale at different stages of the wood fabrication process, including the Natural Wood starting material, Shrunken Wood intermediate, and Moldable Wood product. The color in Fig. S8A represents the maximum principal strain of the fibers and clearly shows the drying process leads to shrinkage, which in turn causes significant buckling of the cell walls. Furthermore, the subsequent partial swelling via the water-shock process of the Shrunken Wood creates unique wrinkles in the cell wall structure of the Moldable Wood. As shown in Fig. S8B, this wrinkled cell wall structure after partial wetting can effectively accommodate severe tension and compression. The resulting strain level in all the cell walls (two right panels of Fig. S8B) is extremely low, with a maximum tensile and compressive strain of 0.47% and 2.66%, respectively, when the Moldable Wood is subjected to a 60% nominal strain (corresponding to the maximum strain level at the outer and inner most parts of the Moldable Wood when it is folded 180˚). Such remarkable strain mitigation is derived from the wrinkled cell wall structure, which can accommodate large elongation and compression by flattening the cell wall wrinkles through cell wall bending instead of pure stretching, and thus results in substantially low strain in the cell walls (*45*).

To further investigate the outstanding foldability and formability of the Moldable Wood, we conducted a comparative simulation of the Non-Moldable Wood (Partially Delignified Wood with ~100 wt.% water content, fabricated without the water-shock process) under a tensile loading condition. As shown in Fig. S8C, there is negligible wrinkling in the cell walls of the Non-Moldable Wood. Meanwhile, under folding-induced elongation of the Non-Moldable Wood in Fig.S8D, the cell walls first straighten along the elongation direction and then are subject to increasing tensile strain upon further elongation. For example, Fig. S8D (middle) shows that under 12.5% overall tension, the maximum principal tensile strain in the cell walls in the Non-Moldable

Wood is as high as 2.3%, significantly higher than the maximum 0.47% principal tensile strain observed in the Moldable Wood at 60% nominal strain. Once the threshold of failure strain is reached, cracks initiate in the highly strained locations in the cell walls of the Partially Delignified Wood and further propagate, causing the material to fail.

Clearly, the Non-Moldable Wood is very brittle and vulnerable to large deformation, which can be understood as follows: The Non-Moldable Wood has a similar porous structure to Natural Wood, with no obvious wrinkled cell wall structures observed after the delignifying and shortened drying process. Our vessel scale modeling in Fig. S7C shows that when folded 180˚, the wood is under both large tensile and compressive strain. As a result, the porous Non-Moldable Wood cannot withstand significant stretching and naturally fractures. In contrast, the water-shock process of the Moldable Wood allows the cell walls to self-wrinkle and preserve space that can accommodate large deformation. Due to this unique porous and wrinkled cell wall structure, the Moldable Wood can sustain both large nominal compressive and tensile strain.

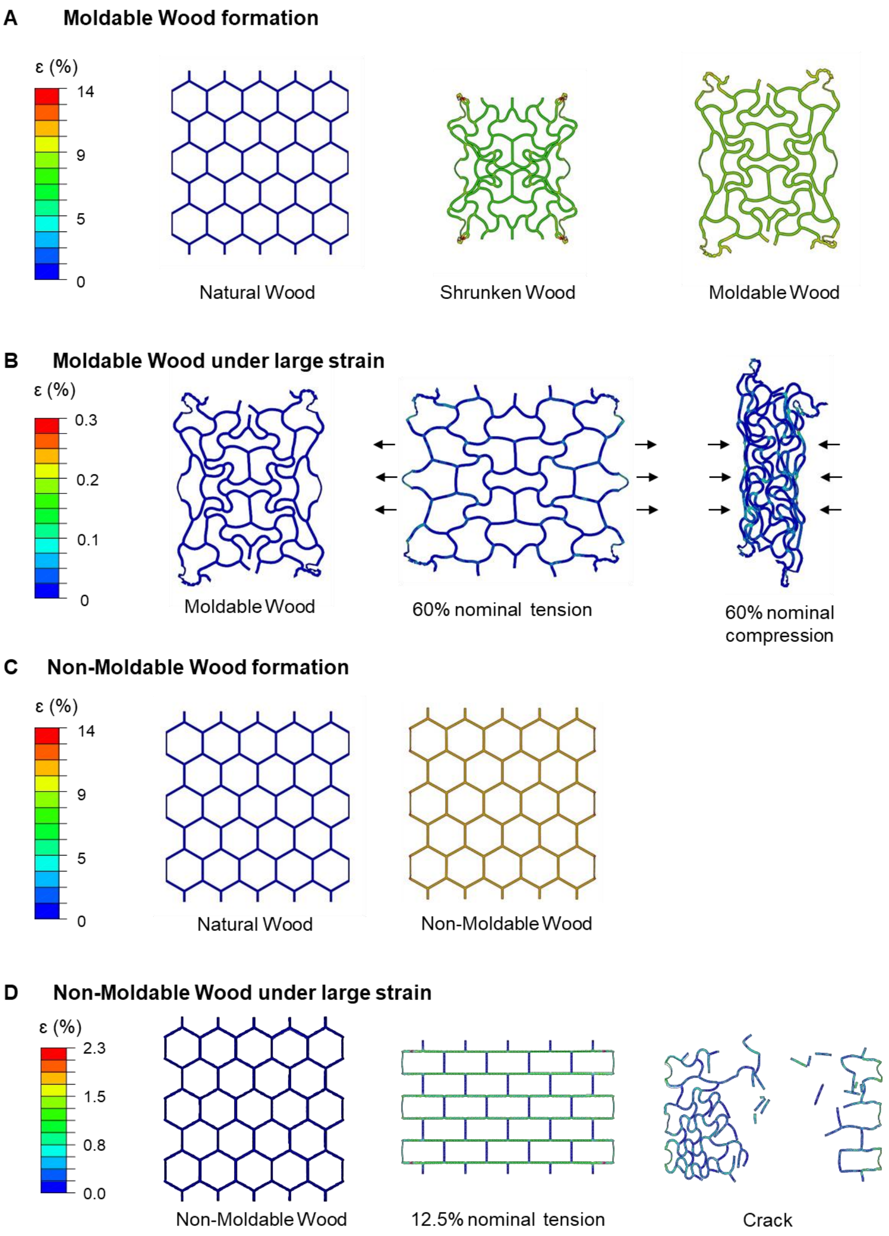

Fig. S8. Foldability modeling of the Moldable Wood vs. Non-Moldable Wood at the fiber scale. (A) Fiber-scale finite element modeling of the Moldable Wood formation. (B) The deformed shapes of the wrinkled cell walls in the Moldable Wood under 60% nominal tension/compression. The modeling results show that even under a large nominal tensile and compressive strain of 60%, the stain level of all cell walls in the Moldable Wood remains extremely low with a low maximum principal tensile and compressive stain of 0.47% and 2.66%, respectively. (C) Fiber-scale finite element modeling of the Non-Moldable Wood formation. (D) (left) The hierarchical structure of the Non-Moldable Wood with an expansion of 6% in the radial direction and 13% in the transverse direction. (middle) The elongated and taut cell walls in the Non-Moldable Wood under 12.5% nominal tension. (right) The collapsed honeycomb network after multiple cracks initiate at highly strained locations when the critical failure strain of the material is reached.

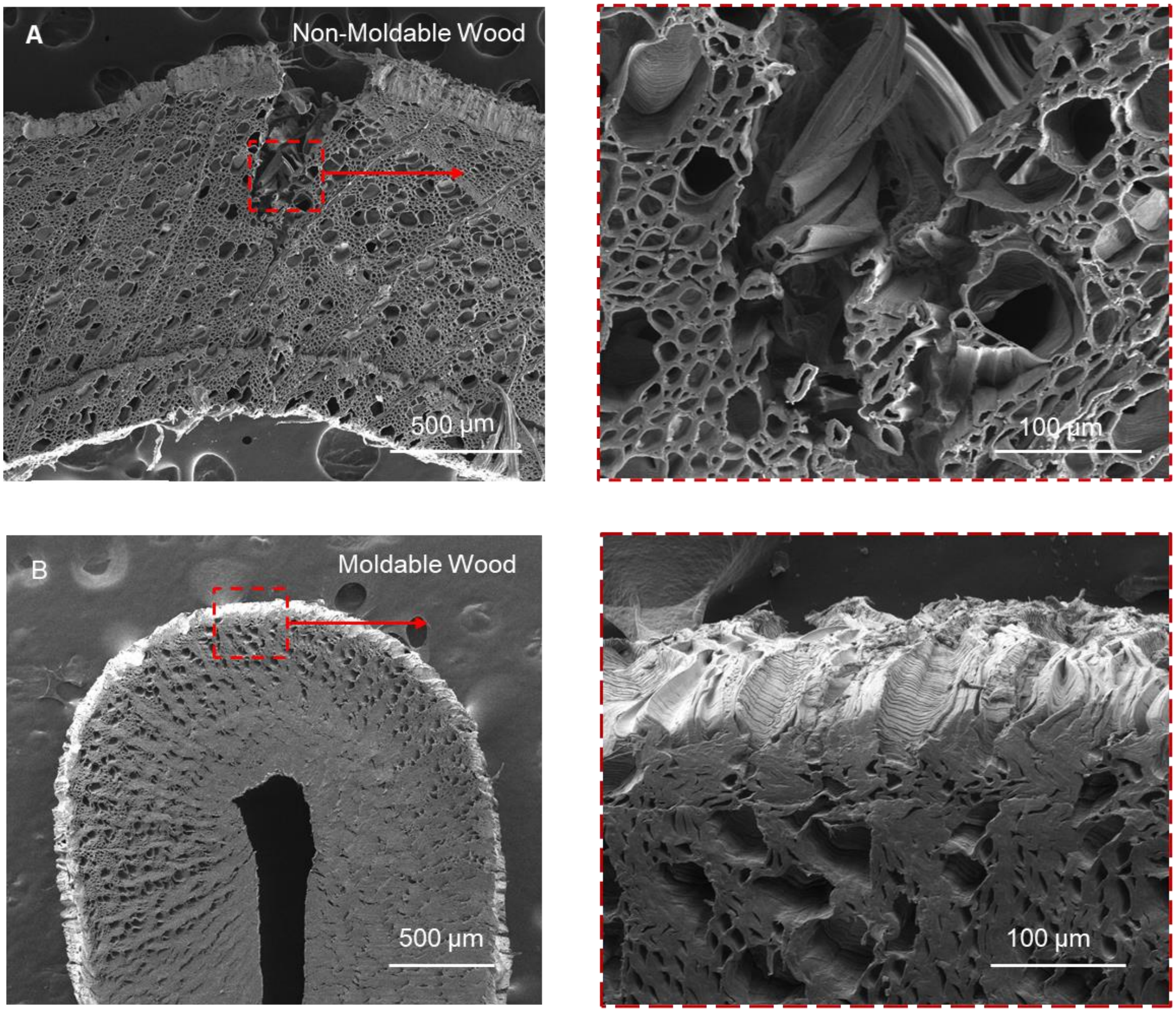

Fig. S9. SEM images of the Non-Moldable Wood and Moldable Wood in the folding state. (A) SEM images of the fractured Non-Moldable Wood after folding. The cell walls separate from each other during folding due to the lack of the wrinkled cell wall structure, which results in little interaction among the fibers. (B) In contrast, the SEM images of the Moldable Wood show the material’s excellent foldability without fracture, which is made possible by the wrinkled cell wall structure that provides both strong interactions between the fibers but also space in the partially opened vessels that can accommodate both tensile and compressive strain.

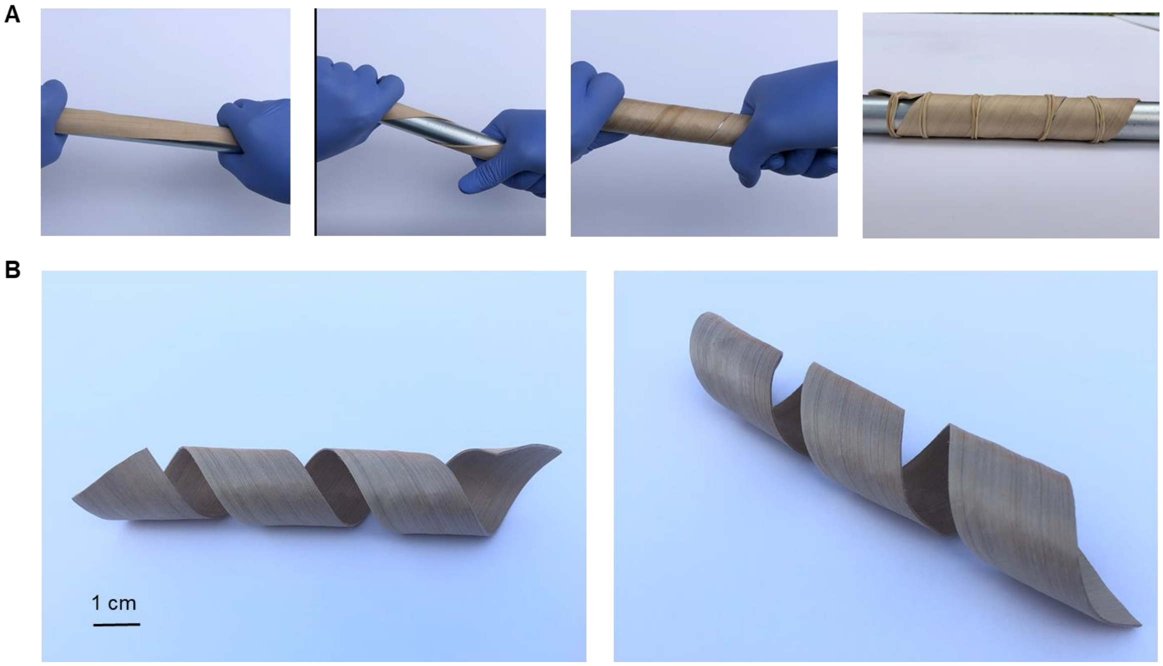

Fig. S10. Preparation of the helical 3D-Molded Wood. (A) The fabrication process of the helical 3D-Molded Wood, in which the Moldable Wood is twisted around a rod, followed by drying to set the structure. (B) Photograph of the resulting helical 3D-Molded Wood.

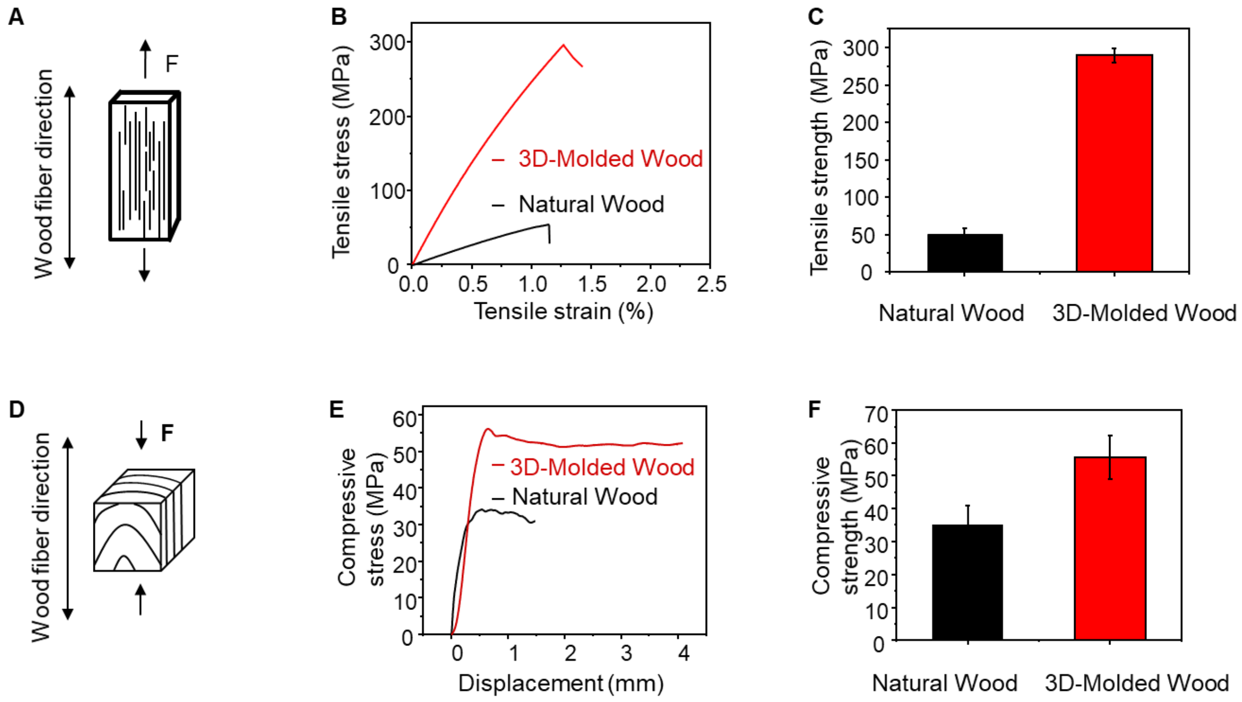

Fig. S11. The mechanical properties of the Natural Wood and 3D-Molded Wood. (A) Schematic of the tensile test along the wood fiber direction. (B) Tensile stress-strain curve of the 3D-Molded Wood and Natural Wood. (C) Tensile strength comparison of the 3D-Molded Wood and Natural Wood. (D) Schematic of the compression test along the wood fiber direction. (E) The compressive stress as a function of displacement for the Natural Wood and 3D-Molded Wood. (F) Comparison of the compressive strength of the Natural Wood and 3D-Molded Wood.

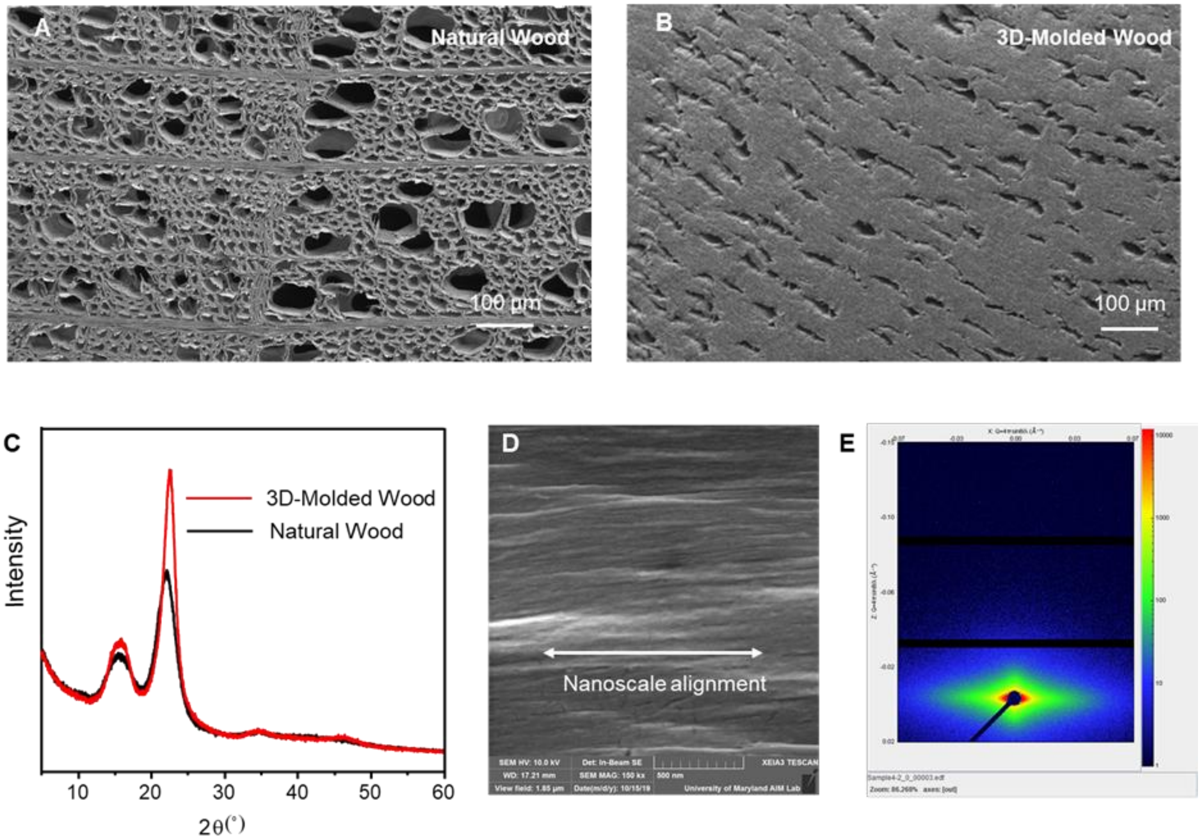

Fig. S12. Characterization of the 3D-Molded Wood at the micro/nanoscale. SEM images of the (A) Natural Wood and (B) 3D-Molded Wood, showing the 3D-Molded Wood has a denser structure than the Natural Wood. (C) XRD patterns of the Natural Wood and 3D-Molded Wood. Note the 3D-Molded Wood has a higher degree of crystallinity than that of the Natural Wood. (D) A high magnification SEM image and (E) small angle X-ray scattering pattern of the 3D-Molded Wood, which indicate the cellulose nanofibers of the 3D-Molded Wood are well-aligned.

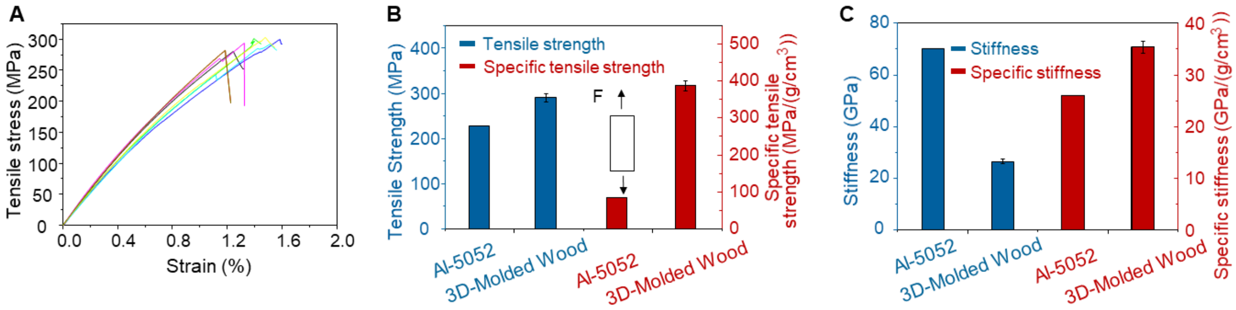

Fig. S13. The mechanical properties of 3D-Molded Wood and Al-5052. (A) The tensile stress-strain curves of the 3D-Molded Wood. Ten measurements were carried out using ten samples. (B) Comparison of the tensile strength and specific tensile strength of the 3D-Molded Wood and Al-5052 (*46*). (C) Comparison of the stiffness and specific stiffness of the 3D-Molded Wood and Al-5052 (*46*). The 3D-Molded Wood features better tensile strength and specific stiffness than those of Al-5052.

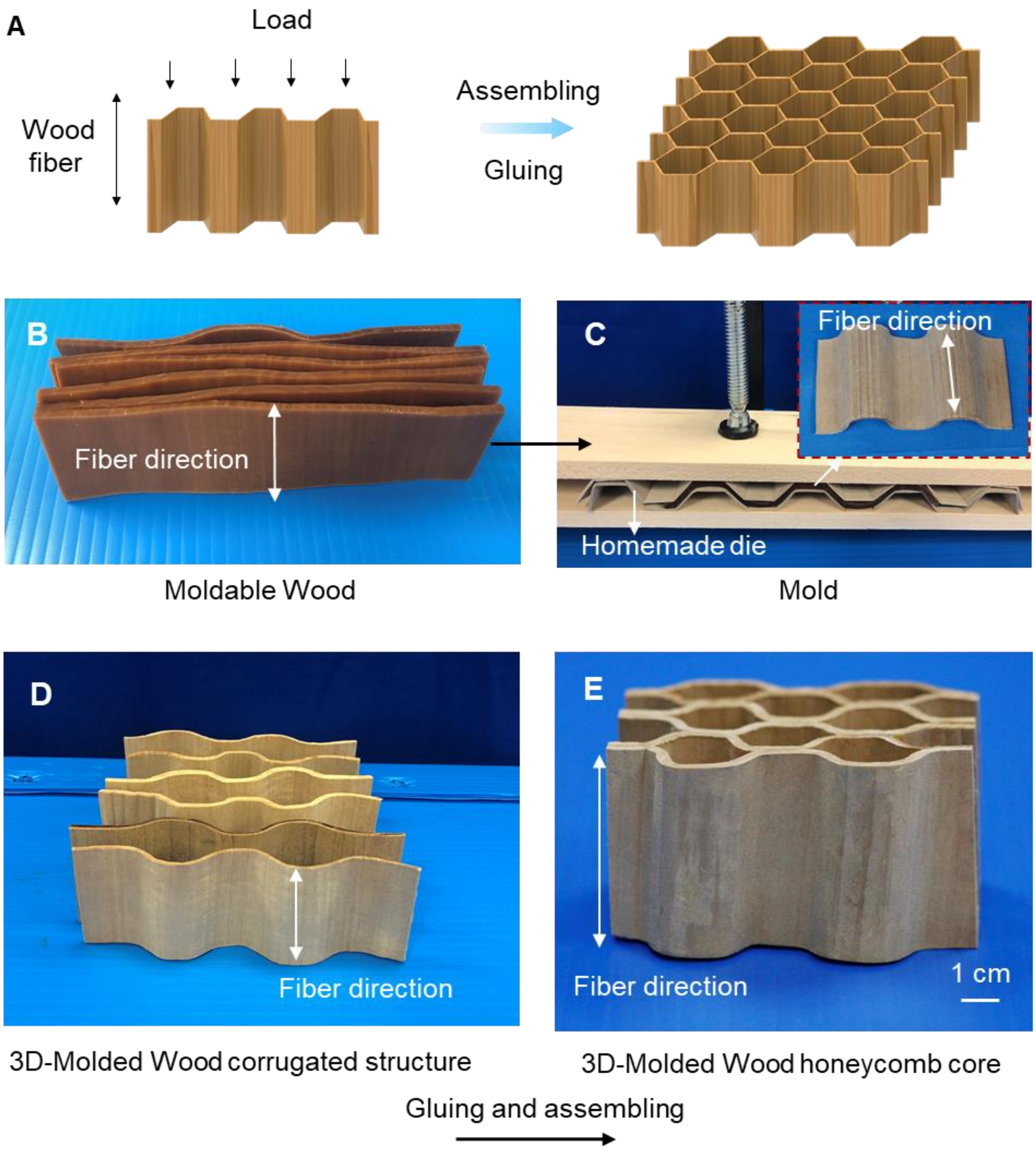

Fig. S14. Preparation of the 3D-Molded Wood honeycomb core material. (A) Schematic showing the preparation of the 3D-Molded Wood honeycomb core. The wood fiber direction is the load-bearing direction, and the mold creases are applied parallel to the wood fibers. (B) Photograph of the Moldable Wood. (C) Photograph of the mold that was used to shape a sheet of the Moldable Wood into a corrugated structure. (D) Photograph of the resulting sheets of corrugated 3D-Molded Wood after water removal from the molded wood. (E) Photograph of the resulting 3D honeycomb core structure after assembling and gluing the corrugated 3D-Molded Wood.

Table S1. Materials cost of the 3D-Molded Wood and Al-5052 plate.

Chemicals	**Reference**	**Price**	**Dosage**	**Total Cost ($\$/m^3$)**
NaOH	Reference (*47*)	300 \$/ton	104 kg	31
Na_2SO_3	Reference (*48*)	300 \$/ton	52 kg	16
Basswood	Reference (*49*)	395 $\$/m^3$	1 m^3	395
Total **(3D-Molded Wood**)				**442**
Al-5052	Reference (*50*)	2300 \$/ton		**6210**

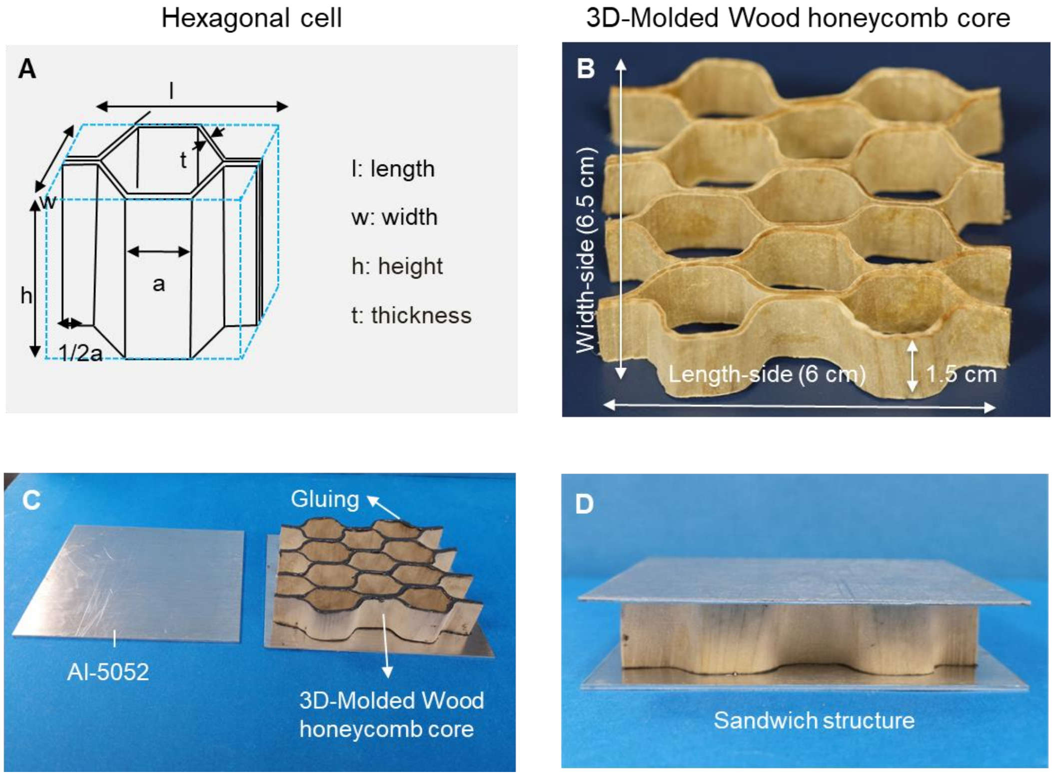

Hexagonal cell

3D-Molded Wood honeycomb core

Fig. S15. The fabrication of the Al-3D-Molded Wood-Al honeycomb core sandwich structure. (A) Schematic of a honeycomb unit. (B) Photograph of the 3D-Molded Wood honeycomb core. (C) Photograph demonstrating the 3D-Molded Wood honeycomb core being glued between two sheets of Al-5052. (D) Photograph of the final Al-3D-Molded Wood-Al honeycomb core sandwich structure.

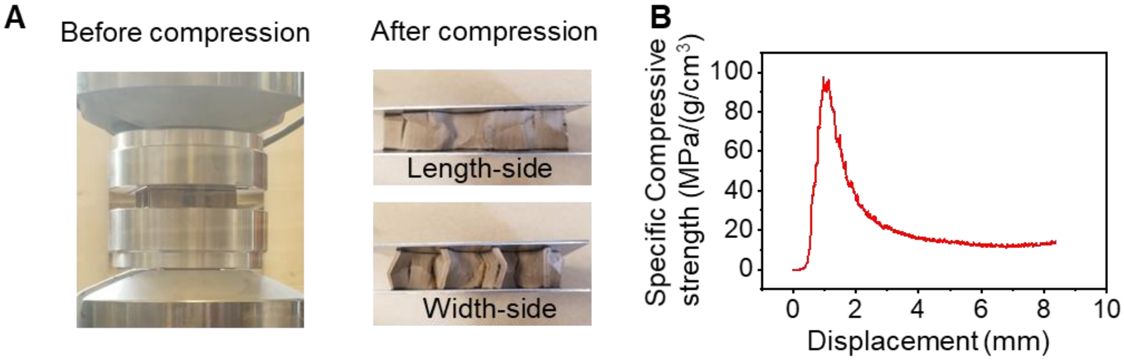

C

Honeycomb core types	Density (g/cm^3)	Compressive strength (MPa)	Specific compressive strength (MPa (g/cm^3))	References
Al-5052 based	0.11	7.8	70.9	(*40*)
Hexagonal glass/phenolic based	0.11	8.4	76.4	(*51*)
Hexagonal glass/polyimide based	0.13	8.3	63.8	(*51*)
Nomex (phenolic) based	0.10	7.8	78.0	(*40*)
Hexagonal carbon/Phenolic based	0.10	6.7	67.0	(*51*)
3D-Molded Wood based	**0.10**	**9.1**	**91.0**	**Our work**

Fig. S16. The compressive strength of the Al-3D-Molded Wood-Al honeycomb core sandwich. (A) Photographs of before and after the compression test of the Al-3D-Molded Wood-Al sandwich. (B) The specific compressive stress-displacement curve of the Al-3D-Molded Wood-Al sandwich. (C) Comparison of the compressive strength of the 3D-Molded Wood honeycomb core with other typical honeycomb core materials (*40*, *51*).

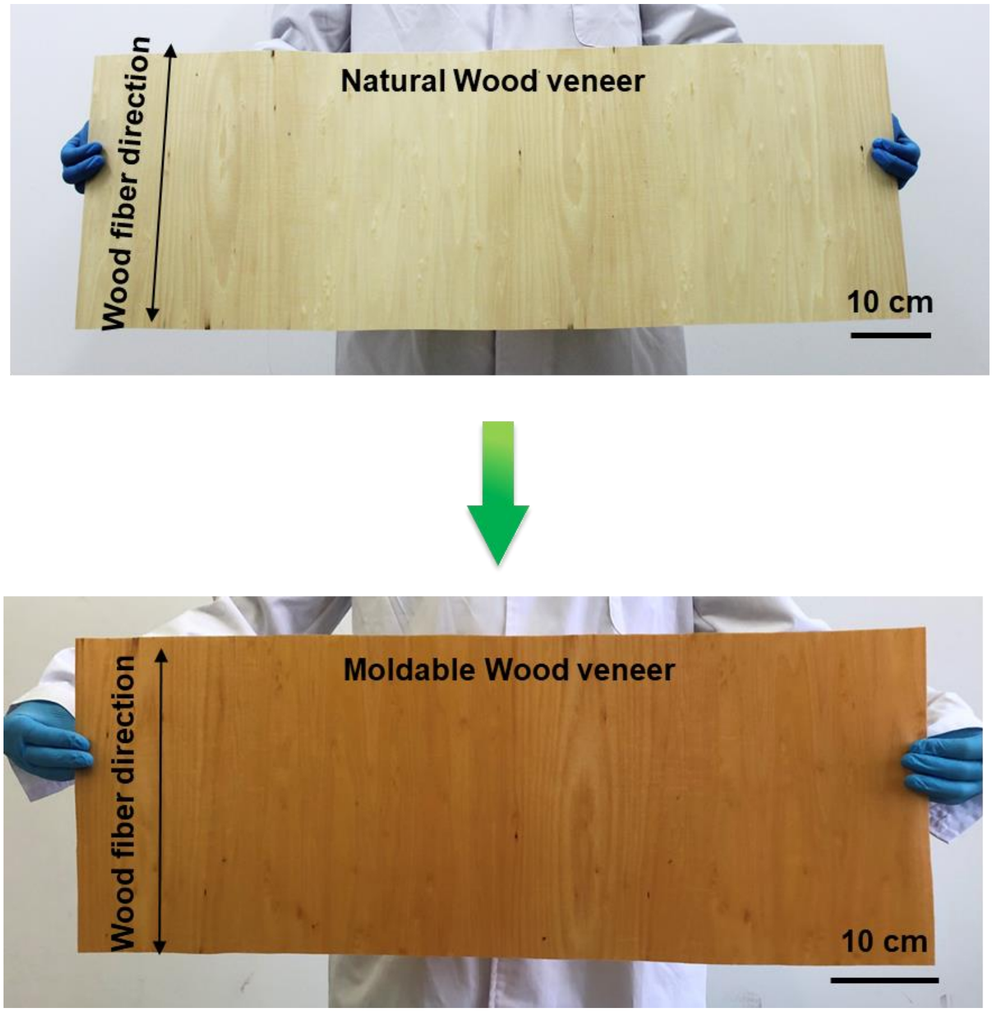

Fig. S17. Large-scale fabrication of Moldable Wood veneer using rotary-cut natural basswood veneer with dimensions of 100 cm (length) by 30 cm (width) by 0.05 cm (thickness) as the starting material.

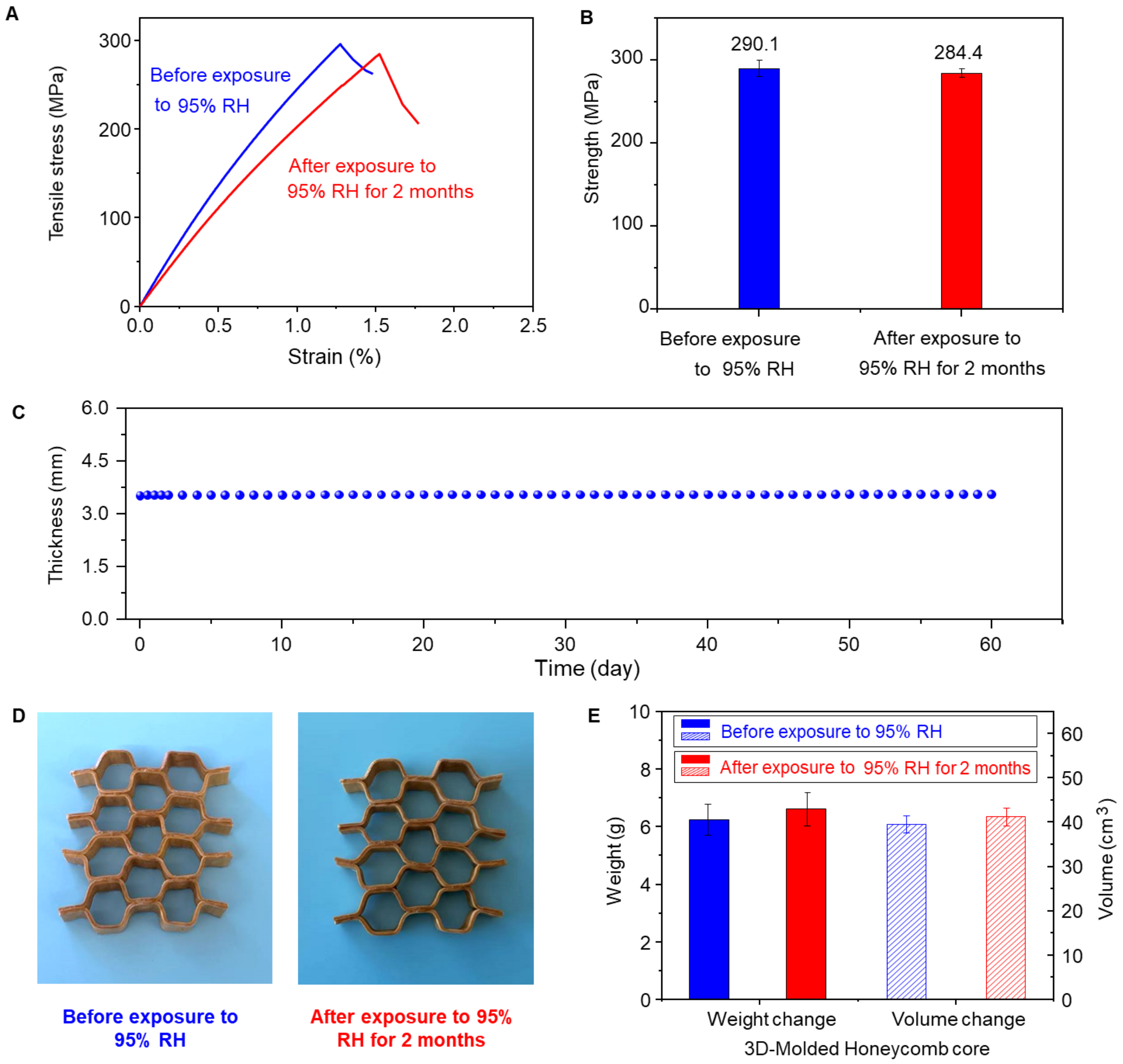

Fig. S18. The stability of the surface-coated (polyurethane coating) 3D-Molded Wood and 3D-Molded Wood honeycomb core before and after exposure to 95% RH for 2 months. (A) The tensile stress-strain curves of the surface-coated 3D-Molded Wood before and after humidity exposure. (B) The tensile strength of the 3D-Molded Wood before (290.1 ± 9.85 MPa) and after (284.4 ± 6.12 MPa) the humidity exposure. (C) Change in the thickness of the surface-coated 3D-Molded over a period of 60 days. (D) Photographs of the surface-coated 3D-Molded Wood honeycomb core before and after the humidity exposure. (E) The weight (before: 6.2563 ± 0.5431 g, after: 6.6143 ± 0.5815 g) and volume (before: 39.60 ± 1.868 cm^3, after: 41.35 ± 2.009 cm^3) of the surface-coated 3D-Molded Wood honeycomb core before and after the humidity exposure.

Table S2. The average weight loss (%) of the Natural Wood, coated Natural Wood, 3D-Molded Wood, and coated 3D-Molded Wood after the fungal decay test.

	Natural Wood	**3D-Molded Wood**	**Coated Natural Wood**	**Coated 3D-Molded Wood**
P. placenta	26.36 ± 5.47	15.02 ± 7.09	18.30 ± 5.24	6.65 ± 1.85
P. chrysosporium	21.05 ± 1.86	5.2 ± 1.14	18.56 ± 3.58	5.42 ± 1.68

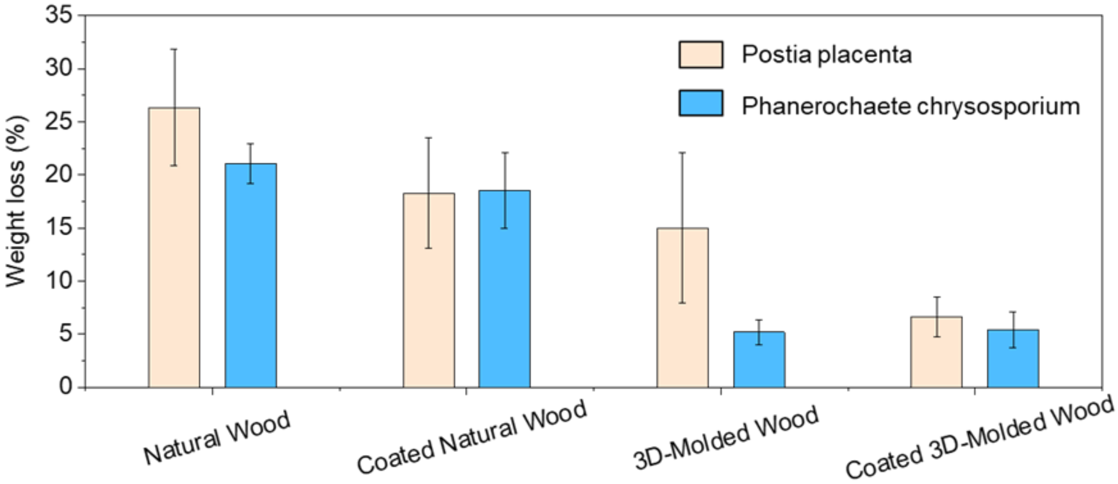

Fig. S19. The anti-fungal property of the polyurethane-coated and uncoated wood samples. The plot shows the average weight loss of the Natural Wood, coated Natural Wood, 3D-Molded Wood, and coated 3D-Molded Wood after the fungal decay test (see Methods for more details). Two wood decay fungi, brown rot fungus *Postia placenta* and white rot fungus *Phanerochaete chrysosporium*, were used to test the degradation susceptibility of the four types of wood samples. The weight loss data shows larger average degradation of the Natural Wood by *P. placenta* (26.36%) and *P. chrysosporium* (21.05%) compared to the 3D-Molded Wood by *P. placenta* (15.02%) and *P. chrysosporium* (5.21%). Similar decay results were obtained for the coated Natural Wood and the coated 3D-Molded Wood by the two fungi (Table S2). Less decay weight losses occurred in the coated Natural Wood (18.3%, 18.56%) compared to the Natural Wood (26.36%, 21.05%) by *P. placenta* and *P. chrysosporium*, respectively. Additionally, the coated 3D-Molded Wood displayed less decay (6.65%) by *P. placenta* compared to the 3D-Molded Wood (15.02%), though no difference was observed in the decay by *P.chrysosporium* with or without the polyurethane coating (5.42% vs 5.21%) (Table S2).

Methodology for Life Cycle Assessment (LCA)

A cradle-to-gate LCA was conducted to compare the environmental impacts of the 3D-Molded Wood with that of aluminum alloy, a traditional metal widely used in the automotive, building, and aircraft industries. The analysis followed the ISO standard 14040 series (*52*) and was conducted using OpenLCA 1.10.3 (*53*). The LCA was first developed for 1 kg (the first functional unit) of 3D-Molded Wood and Al alloy, then the results were converted to the second functional unit based on the specific tensile strength (see Equation S2 for details) and third functional unit based on the specific stiffness (see Equation S8 for details). This approach was adapted from a recent LCA study of composite material (*54*). The importance of considering material properties, such as strength, in LCAs has been widely recognized (*55*). The system boundary included raw material acquisition, transportation, and production. The Life Cycle Inventory (LCI) data included the primary data collected from experiments for the 3D-Molded Wood production (Tables S3 and S7), and the secondary data collected from the Ecoinvent 3.5 database (*56*) and literature (*57*). The Life Cycle Impact Assessment (LCIA) was performed using the TRACI method developed by the U.S. Environmental Protection Agency (*58*).

The LCI data of the production stage of the 3D-Molded Wood is shown in Table S3. A process flow diagram is provided in Fig. S20. The LCI data of cultivation, logging, sawing, and drying of basswood lumber were collected from a previous LCA report for U.S. hardwood lumber (*57*). The LCI data of the upstream production of chemicals, electricity, and water, as well as the metal Al alloy were collected from the Ecoinvent 3.5 database (*56*). Specifically, the LCI of the upstream production of NaOH was modeled based on the NaOH produced from chlor-alkali electrolysis using a diaphragm cell, the dominant process used in North America (*59*), and the system boundary included all upstream activities starting from salt mining. The electricity grid was set to the United States. The LCI of upstream production of Na_2SO_3 was modeled based on the Na_2SO_3 production, which treats a suspension of sodium hydroxide with sulfur dioxide made from sulfur. Sulfur is usually recovered from oil refineries and natural gas plants, the upstream of which are included and labeled as "Extraction of Raw Materials" in Fig. S20 (e.g., the extraction of oil is included for sulfur coming from oil refineries and the extraction of natural gas is included for sulfur coming from a natural gas plant). Similar to the NaOH modeling, the system boundary includes all upstream activities, and the electricity and heat was modeled for the United States. As electricity and heat are used in most unit processes, they are listed in a separate box in Fig. S20 to avoid duplications for each unit process. However, we plot the upstream activities of electricity supplied to wood pretreatment as an example to show how upstream activities of electricity were included in this LCA. Similarly, transportation is needed between different unit processes and is listed separately as a single box in Fig. S20 to avoid duplications. The LCI of the electricity grid in the United States includes a mix of different electricity generation technologies, such as coal, natural gas, renewables, and nuclear. The LCI of upstream tap water production and distribution was modeled based on the market mix of tap water production technologies in North America. We set the water loss in the distribution network specifically to the United States (10%) (*60*).

Both the lumber and chemicals were assumed to be transported by truck, and the distances were 312 km and 352 km, respectively, based on the average distances of truck transportation for wood products and basic chemicals in the United States in 2017 (*61*). The truck was assumed to be a diesel-powered combination truck, and the LCI data of the transportation and upstream production of fuels was collected from the U.S. Life Cycle Inventory database (*62*). The LCI data for all upstream production activities of the Al alloy included both primary and secondary Al (made from Al scrap). The LCI data for the upstream production and transportation activities of the Al alloy was modeled based on the global production of Al alloy containing 3% magnesium by mass in Ecoinvent (*56*). The electricity and fuels were set to the United States to be consistent with the LCI model of the 3D-Molded Wood. The global dataset in Ecoinvent reports that 26.1% of Al alloy is from primary production and the 73.9% of Al alloy is from Al alloy scrap. This data was used to present the results shown in Fig. 4G, and 73.9% is a high estimation of recycled contents of Al alloy product and the percentage for the United States could be lower. The recycling rate of Al alloy reported by the U.S. Environmental Protection Agency was 50.4% for Al alloy cans but as low as 35% of the total Al alloy waste generated (*63*). To better understand the impacts of recycled contents, we also modeled an additional scenario for Al alloy using 35% recycled contents (as a low recycled content scenario in contrast to the high recycled content scenario mentioned previously).

Table S3. Inputs and outputs of the 3D-Molded Wood production process presented in this work.

Inputs/Outputs	Quantity	Unit
Step 1: Wood treatment (wood samples were treated with a boiling chemical delignification solution for 48 hours, followed by immersion in water several times and then the samples were air dried at room temperature for 30 hours to form the Shrunken Wood).[a]		
Input		
Basswood[a]	825	g
NaOH	200	g
Na_2SO_3	100	g
Energy[b]	4.19	kWh
Water	2000	g
Output		

Shrunken Wood (~12 wt.% water content, see Fig. S4)	663	g
Wastewater[d]	621	g
Step 2: Wood re-wetting (water-shock) and drying at room temperature		
Input		
Shrunken Wood	663	g
Water (for wood re-wetting)	517	g
Output[e]		
3D-Molded Wood (after air-dried at room temperature) [c]	636–687	g

[a] Chemicals (NaOH and Na_2SO_3) were added to water for the delignification solution that was used to treat the Natural Wood blocks. 825 g wood mass are for 10 wood samples treated.

[b] Electricity is used for heating in the wood treatment process. The LCI data of the electricity generation are collected from the Ecoinvent database (*56*) based on the U.S. electricity mix that includes the electricity generated by different processes (e.g., coal, natural gas, petroleum, renewable, and nuclear) across the nation.

[c] The size of the 3D-Molded Wood was 29.4 cm by 12.3 cm by 0.244 cm, the density of the 3D-Molded Wood was 0.75 ± 0.029 g/cm³.

[d] This wastewater contains NaOH, Na_2SO_3, lignin and hemicellulose. NaOH and Na_2SO_3 were modeled as elementary flow (output to nature), which were included in the LCIA. Lignin and hemicellulose are natural components of biomass and can be biodegraded (*64, 65*). Therefore, lignin and hemicellulose in this wastewater stream were assumed to have no environmental impact in the LCIA.

[e] In Step 2, water was added to increase the water mass ratio of the Shrunken Wood (~12 wt.% water content) to Moldable Wood (~100 wt.% water content) for the water-shock process, see Fig. S4 for the changes of the water mass ratio. Water adsorbed by the Moldable Wood then evaporated when drying at room temperature. Additional water remaining after the water-shock process was re-used to treat the next wood sample instead of being disposed. Therefore, no water was disposed as liquid, which explains why no wastewater was generated in Step 2.

The LCIA results of the 3D-Molded Wood were compared with Al alloy (containing 3% magnesium by mass). The LCIA results were first calculated for 1 kg of 3D-Molded Wood and Al alloy, then the results were converted to the second functional unit that takes the specific tensile strength into consideration, as shown in Equation S2:

$$EI_{p'} = \frac{EI_p}{\sigma'_p} \times \frac{1}{1000} \qquad \text{(Equation S2)}$$

where EI_p is the environmental impact of the material (per kg of 3D-Molded Wood or Al alloy) and $EI_{p'}$ is the environmental impact of the material (per cm^3 per MPa) converted from EI_p using the specific tensile strength (σ'_p in the unit of MPa/(g/cm^3)). 1000 is for unit conversion from kg to g. Using the mass as the functional unit is very common in LCAs for different materials; however, such a functional unit does not take material property into consideration (*54*). To meet the strength requirement of the same application, one material with higher strength would need less mass than the other material with lower strength. Therefore, merely comparing the environmental impacts of different materials based on a constant mass could be misleading. The specific tensile strength of the 3D-Molded Wood and Al alloy in this study were 386.8 ± 13.13 MPa/(g/cm^3) and 84.4 MPa/(g/cm^3), respectively. The same strength data were used to calculate the mass ratio that reflects how much 3D-Molded Wood would be needed in mass to fulfill the same strength requirements provided by the Al alloy. We define σ_w as the tensile strength of the 3D-Molded Wood, σ_{AI} as the tensile strength of the Al alloy, and A_w and A_{AI} are the cross-sectional areas for the wood and Al alloy used in the same application. We can then obtain the following equations:

$$\sigma_w = \frac{F}{A_w} \qquad \text{(Equation S3)}$$

$$\sigma_{AI} = \frac{F}{A_{AI}} \qquad \text{(Equation S4)}$$

The force F in the two equations should be equal for materials that can provide the same strength:

$$\frac{\sigma_w}{\sigma_{AI}} = \frac{A_{AI}}{A_w} \qquad \text{(Equation S5)}$$

For two materials used in the same application, the length/height (l) should be the same, thus the ratio of σ_w to σ_{AI} can be transformed as:

$$\frac{\sigma_w}{\sigma_{AI}} = \frac{A_{AI}l}{A_w l} = \frac{V_{AI}}{V_w} = \frac{\rho_w}{\rho_{AI}} \times \frac{M_{AI}}{M_w} \qquad \text{(Equation S6)}$$

where ρ_w and ρ_{AI} are the density of the 3D-Molded Wood and Al alloy, respectively. The mass ratio of the two materials can be further derived as:

$$\frac{M_w}{M_{AI}} = \frac{\sigma_{AI}}{\sigma_w} \times \frac{\rho_w}{\rho_{AI}} = \frac{\sigma'_{AI}}{\sigma'_w} \qquad \text{(Equation S7)}$$

where σ'_{AI} and σ'_w are the specific tensile strength of the 3D-Molded Wood and Al alloy.

Another material property measured in this study is the stiffness of both 3D-Molded Wood and Al alloy. To take stiffness into consideration, the LCIA results were normalized using Equation S8 to estimate the ratio of the environmental impacts per cm^3 to specific stiffness. σ'_s is the specific stiffness in the unit of GPa/(g/cm³). 1000 is for unit conversion from kg to g. The stiffness data are 35.36 ± 1.196 GPa/(g/cm^3) for 3D-Molded Wood and 26.03 Gpa/(g/cm^3) for Al alloy (Fig. S13).

$$EI_{s\prime} = \frac{EI_p}{\sigma'_s} \times \frac{1}{1000} \qquad \text{(Equation S8)}$$

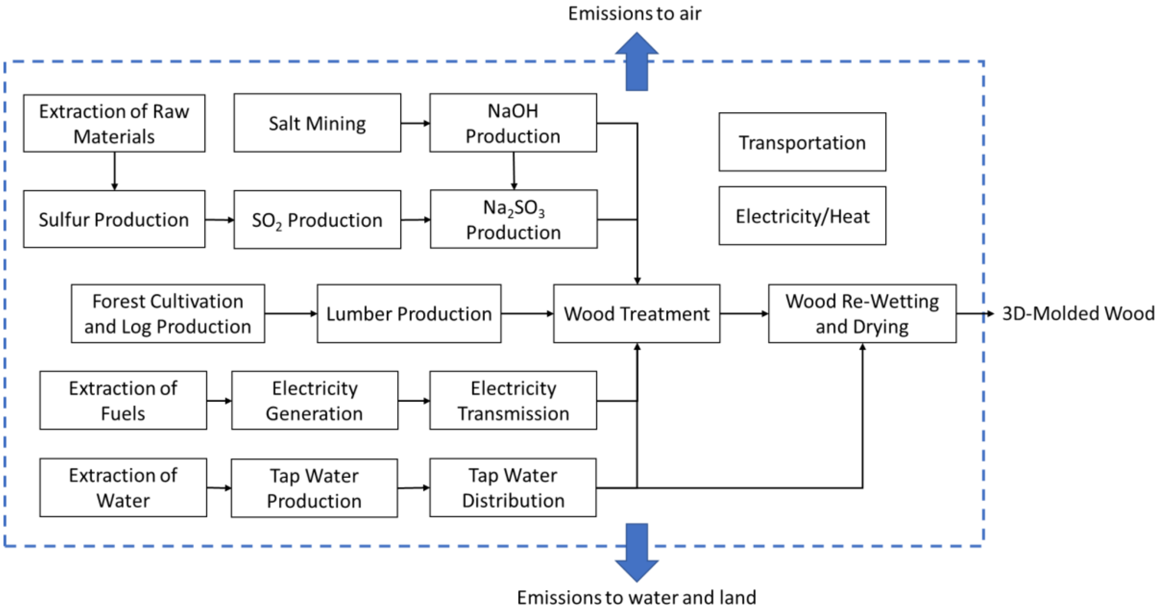

Fig. S20. The process flow diagram of the LCA system boundary.

LCA Results and Discussion

The environmental impacts of the 3D-Molded Wood are shown in Table S4. The results are presented on the basis of three functional units, one is the mass as 1 kg (as EI_p in Equation S2), the other two are per cm^3/MPa (as $EI_{p\prime}$ in Equation S2) and per cm^3/GPa (as $EI_{s\prime}$ in Equation S8). As discussed previously, comparing different materials solely on the basis of mass could be misleading, given the differences in material properties that have direct impacts on the functionality provided by the materials. Thus, the results per kg are provided here for documentation purposes rather than providing a direct comparison.

Table S4. The environmental impacts of 3D-Molded Wood on the basis of mass (per kg) and material properties (per cm^3/MPa for strength and per cm^3/GPa for stiffness)

Environmental impact categories	**Unit of impact category**	EI_p **Impact per kg**		EI'_p **Impact per cm^3/MPa**		EI'_s **Impact per cm^3/GPa**	
		Min	**Max**	**Min**	**Max**	**Min**	**Max**
Acidification	kg SO_2 eq	2.30×10^{-2}	2.48×10^{-2}	5.74×10^{-8}	6.64×10^{-8}	6.28×10^{-7}	7.26×10^{-7}
Human health - carcinogenics	CTUh	3.92×10^{-7}	4.23×10^{-7}	9.79×10^{-13}	1.13×10^{-12}	1.07×10^{-11}	1.24×10^{-11}
Ecotoxicity	CTUe	39.2	42.3	9.80×10^{-5}	1.13×10^{-4}	1.07×10^{-3}	1.24×10^{-3}
Eutrophication	kg N eq	3.59×10^{-2}	3.88×10^{-2}	8.97×10^{-8}	1.04×10^{-7}	9.81×10^{-7}	1.13×10^{-6}
Fossil fuel depletion	MJ surplus	4.90	5.29	1.22×10^{-5}	1.42×10^{-5}	1.34×10^{-4}	1.55×10^{-4}
Global warming potential	kg CO_2 eq	5.51	5.96	1.38×10^{-5}	1.59×10^{-5}	1.51×10^{-4}	1.74×10^{-4}
Human health - non-carcinogenics	CTUh	1.45×10^{-6}	1.57×10^{-6}	3.63×10^{-12}	4.20×10^{-12}	3.97×10^{-11}	4.59×10^{-11}
Ozone depletion	kg CFC-11 eq	6.67×10^{-7}	7.20×10^{-7}	1.67×10^{-12}	1.93×10^{-12}	1.82×10^{-11}	2.11×10^{-11}
Respiratory effects	kg PM2.5 eq	1.71×10^{-2}	1.85×10^{-2}	4.27×10^{-8}	4.94×10^{-8}	4.67×10^{-7}	5.40×10^{-7}
Smog formation	kg O_3 eq	2.61×10^{-1}	2.82×10^{-1}	6.53×10^{-7}	7.55×10^{-7}	7.15×10^{-6}	8.26×10^{-6}

CTUe: comparative toxicity unit for ecotoxicity. CTUh: comparative toxicity unit for human health. CFC-11eq: CFC-11 (trichlorofluoromethane) equivalent. PM2.5 eq: particulate matter 2.5 equivalent.

Table S5. The environmental impacts of Al alloy on the basis of mass (per kg) and material properties (per cm^3/MPa for strength and per cm^3/GPa for stiffness)

Environmental impact categories	Unit of impact category	EI_p Impact per kg		EI_p' Impact per cm^3/MPa		EI_s' Impact per cm^3/GPa	
		HRS*	**LRS****	**HRS**	**LRS**	**HRS**	**LRS**
Acidification	kg SO_2 eq	3.54×10^{-2}	6.96×10^{-2}	4.19×10^{-7}	8.25×10^{-7}	1.36×10^{-6}	2.67×10^{-6}
Human health - carcinogenics	CTUh	1.65×10^{-6}	3.15×10^{-6}	1.96×10^{-11}	3.73×10^{-11}	6.36×10^{-11}	1.21×10^{-10}
Ecotoxicity	CTUe	2.01×10^{3}	1.16×10^{3}	2.38×10^{-2}	1.38×10^{-2}	7.72×10^{-2}	4.46×10^{-2}
Eutrophication	kg N eq	2.94×10^{-2}	4.61×10^{-2}	3.48×10^{-7}	5.46×10^{-7}	1.13×10^{-6}	1.77×10^{-6}
Fossil fuel depletion	MJ surplus	3.98	6.55	4.71×10^{-5}	7.76×10^{-5}	1.53×10^{-4}	2.52×10^{-4}
Global warming potential	kg CO_2 eq	6.98	13.0	8.27×10^{-5}	1.54×10^{-4}	2.68×10^{-4}	4.98×10^{-4}
Human health - non-carcinogenics	CTUh	3.84×10^{-6}	4.62×10^{-6}	4.55×10^{-11}	5.47×10^{-11}	1.47×10^{-10}	1.77×10^{-10}
Ozone depletion	kg CFC-11 eq	3.66×10^{-7}	5.91×10^{-7}	4.34×10^{-12}	7.00×10^{-12}	1.41×10^{-11}	2.27×10^{-11}
Respiratory effects	kg PM2.5 eq	1.22×10^{-2}	1.88×10^{-2}	1.44×10^{-7}	2.23×10^{-7}	4.68×10^{-7}	7.22×10^{-7}
Smog formation	kg O_3 eq	4.06×10^{-1}	7.85×10^{-1}	4.81×10^{-6}	9.30×10^{-6}	1.56×10^{-5}	3.02×10^{-5}

*HRS: the high recycling scenario based on the global data in Ecoinvent (*56*), which indicates that 26.1% of Al alloy is from primary production and 73.9% is from Al alloy scrap.

**LRS: the low recycling scenario, which assumes the Al alloy recycling content is as low as 35%, based on the U.S. data (*63*).

The comparative results of the 3D-Molded Wood and Al alloy based on the tensile strength are shown in Fig. S21 for Al alloy in the low recycling scenario (the high recycling scenario is shown in Fig. 4G). Compared with Al alloy in both the high and low recycling scenarios, 3D-Molded Wood shows remarkable environmental reduction across all impact categories (59–99% reduction compared with Al alloy in the high recycling scenario, as shown in Fig. 4G, and 74–99% reduction compared with Al alloy in the low recycling scenario, as shown in Fig. S21).

Fig. S22 and Fig. S23 are environmental impact comparison based on the specific stiffness for Al alloy in the low and high recycling scenario, respectively. 3D-Molded Wood showed significant reductions across all impact categories compared with Al alloy in the low recycling scenario (14–97% reduction, Fig. S22). Compared with Al alloy in the high recycling scenario (Fig. S23), 3D-Molded Wood has lower environmental impacts in most categories (40–99% lower) except eutrophication and fossil fuel depletion (where 3D-Molded Wood are close to Al alloy), and ozone depletion and respiratory effects (where 3D-Molded Wood was slightly higher than Al alloy).

We conducted a contribution analysis to understand the major contributors to the environmental impacts of the 3D-Molded Wood developed in this study. The results are shown in Table S6 and organized by input materials (except transportation, which includes transporting basswood and the necessary chemicals). The contributions of water, transportation, and basswood to some environmental impact categories are almost negligible, therefore shown as zero after rounding down.

Table S6. Results of the contribution analysis.

	Basswood	**NaOH**	**Na_2SO_3**	**Energy**	**Water**	**Transportation**	**Total**
Acidification	15.0%	9.2%	21.7%	53.9%	0.0%	0.1%	100%
Human health - carcinogenics	0.1%	7.8%	4.8%	87.1%	0.2%	0.0%	100%
Ecotoxicity	0.2%	10.7%	7.3%	81.7%	0.0%	0.0%	100%
Eutrophication	0.9%	5.4%	3.2%	90.5%	0.0%	0.0%	100%
Fossil fuel depletion	25.7%	6.5%	7.9%	58.1%	0.0%	1.7%	100%
Global warming potential	14.3%	8.0%	4.5%	72.3%	0.0%	0.9%	100%
Human health - non-carcinogenics	2.1%	10.6%	8.1%	78.9%	0.0%	0.1%	100%

Ozone depletion	0.0%	35.7%	14.7%	49.5%	0.0%	0.0%	100%
Respiratory effects	21.0%	4.2%	3.4%	71.4%	0.0%	0.0%	100%
Smog formation	43.6%	9.9%	5.7%	40.6%	0.0%	0.1%	100%

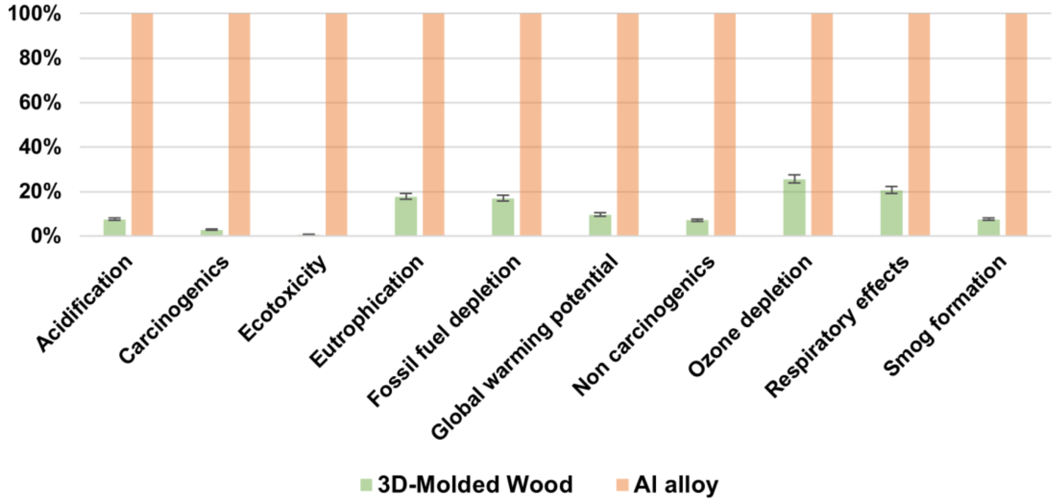

Fig. S21. Environmental impacts per cm^3/MPa based on the specific tensile strength for 3D-Molded Wood prepared using the 48-hour delignification treatment in **Table S3**, normalized to the higher impact material for each environmental impact category (Al alloy in the low recycling scenario with 35% recycled content).

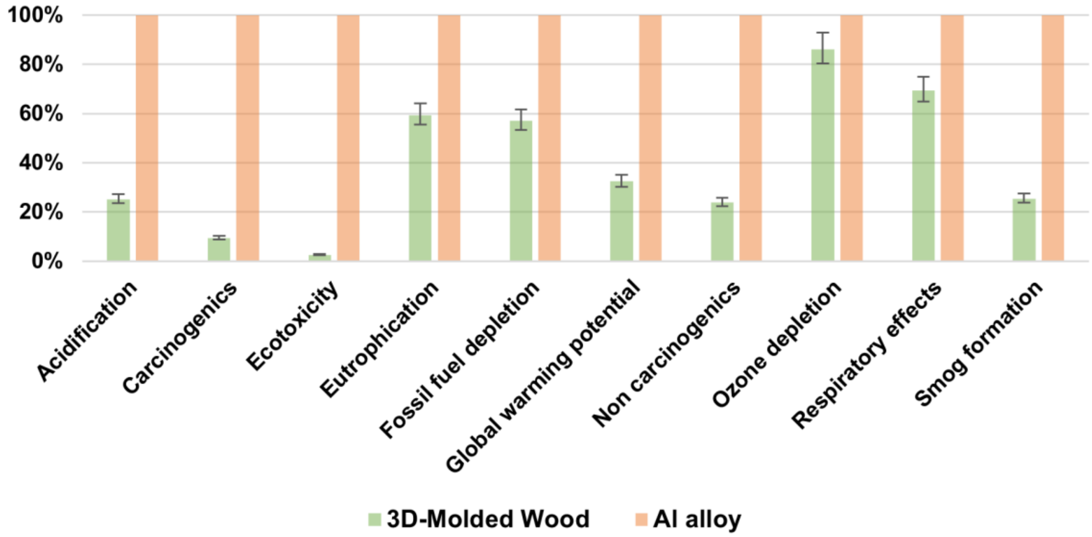

Fig. S22. Environmental impacts per cm^3/GPa based on the specific stiffness for 3D-Molded Wood prepared from 48-hour delignification treatment in **Table S3**, normalized to the higher impact material for each environmental impact category (Al alloy in the low recycling scenario with 35% recycled content).

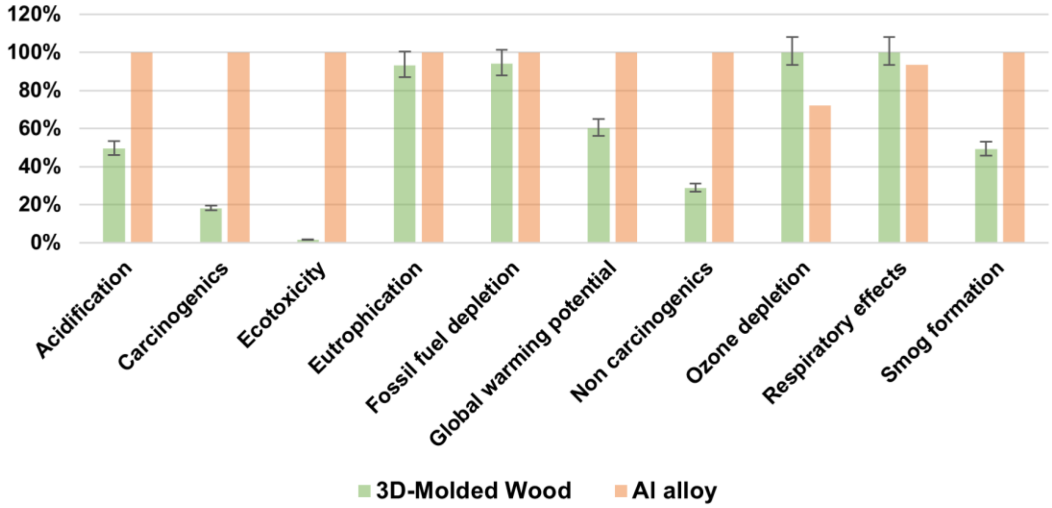

Fig. S23. Environmental impacts per cm^3/GPa based on the specific stiffness for 3D-Molded Wood prepared from the 48-hour delignification treatment in **Table S3**, normalized to the higher impact material for each environmental impact category (Al alloy in the high recycling scenario with 73.9% recycled content).

Given the large impacts of energy consumption during the wood treatment, we tested a strategy to reduce the energy consumption by decreasing the wood delignification time from 48 hours to only 15 mins (Fig. S24). 20 pieces of Natural Wood sheets were treated with a boiling aqueous solution of NaOH and Na_2SO_3 for 15 mins, followed by immersion in water several times to remove the chemicals (and this water was re-used for the next wood treatment). The Partially Delignified Wood was air dried at room temperature for 30 hours to form the Shrunken Wood that was then re-wetted for 3 mins (i.e., the water-shock process) to form the Moldable Wood. The Moldable Wood was shaped into the desired structure and air-dried at room temperature for 30 hours to produce the 3D-Molded Wood. The tensile strength and stiffness of the 3D-Modeled Wood treated by this strategy were 289 ± 6.92 MPa and 24.32 ± 1.10 GP, respectively. The density of the 3D-Molded Wood was 0.80 ± 0.04 g/cm^3.

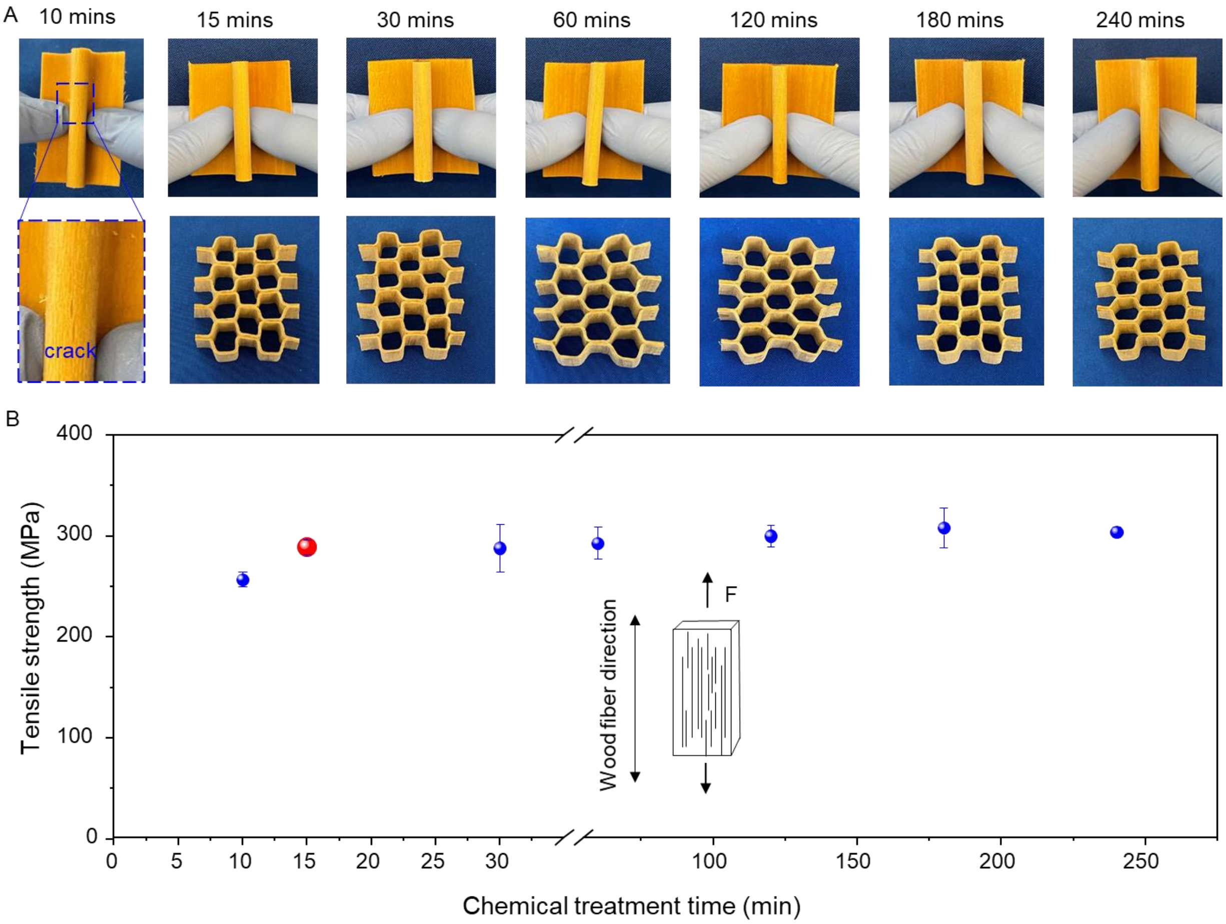

Fig. S24. Decreasing the delignification (chemical treatment) time from 48 hours to 15 mins without sacrificing the performance. (A) Photographs of the Moldable Wood samples and the corresponding 3D-Molded Wood honeycomb structures obtained by various chemical delignification treatment times (10–240 mins) under 180° of folding, all demonstrating excellent foldability and moldability except the sample obtained from 10-min delignification treatment. (B) The influence of the delignification treatment time on the tensile strength of the final 3D-Molded Wood product, showing that the treatment time can be shortened from 240 mins to 15 mins without sacrificing the mechanical strength of the 3D-Molded Wood.

The LCI data of this strategy are provided in Table S7 and an additional LCA was conducted to understand the impacts of the decreased wood delignification time.

Table S7. Inputs and outputs of the 3D-Molded Wood production process with the shortened wood delignification time (15 mins).

Inputs/Outputs	Quantity	Unit
Step 1: Wood treatment (wood samples were treated with a boiling chemical delignification solution for 15 mins, followed by immersion in water several		

times and then the samples were air dried at room temperature for 30 hours to form the Shrunken Wood).[a]		
Input		
Basswood[a]	4055	g
NaOH	200	g
Na_2SO_3	100	g
Energy	1.1	kWh
Water[b]	6800	g
Output		
Shrunken Wood (12 wt.% water content,see Fig. S4)	3550	g
Wastewater[c]	1100	g
Step 2: Wood re-wetting (water-shock) and drying at room temperature		
Input		
Shrunken Wood	3550	g
Water (for wood re-wetting)	2770	g
Output[d]		
3D-Molded Wood (after air-driedat room temperature)[c]	3370-3725	g

[a] NaOH and Na_2SO_3 were added to water to form the chemical delignification solution. 20 pieces of Natural Wood blocks (basswood, typical sample dimensions: 1.58 mm x 30 cm x 20 cm) were treated each time, and the chemical solution was re-used 4 times. 20 pieces were treated the first time, and another 80 pieces were treated by re-using the solution, treating a total of 100 pieces of wood (4055 g). Note that a 1.58 mm thick wood sheet is a typical veneer thickness in the wood industry.

[b] The water consumption includes 2000 g of water used for the first time and 4800 g of water added in the re-used chemical solution (4 times of re-use with 1200 g water added each time). In each treatment, the wood samples adsorbed a large amount of water (see the increased water mass ratio of the Partially Delignified Wood in Fig. S4), resulting in a residual chemical solution that has a reduced amount of water compared to the original chemical delignification solution. 1200 g of water was used to wash the Partially Delignified Wood and added to the residual chemical solution for re-use. The water adsorbed by the Partially Delignified Wood evaporates during air drying, which explains why the amount of wastewater disposed (after 4 times of re-use) is much smaller than the water input.

[c] The size of the 3D-Molded Wood was 29.8 cm × 12.4 cm × 0.12 cm, the density of the 3D-Molded Wood was 0.80 ± 0.04 g/cm³.

[d] In Step 2, water was added to increase the water mass ratio of the Shrunken Wood (~12 wt.% water content) to Moldable Wood (~100 wt.% water content) in the re-wetting (water-shock) process. See Fig. S4 for the changes in the water mass ratio. Then water absorbed by the Moldable Wood evaporates when drying at room temperature. The remaining water from the water-shock treatment can be reused many times without limit as it is relatively pure, without any chemical contamination or chemical reaction taking place during the water-shock process. Therefore, no water is disposed as liquid in this step, which explains why no wastewater is listed for Step 2.

As 3D-Molded Wood was surface coated with polyurethane (PUR) to address the durability issues, one additional LCA was conducted to include PUR. The LCI data of the upstream production of the PUR coating were collected from the Evah OzLCI2019 database through the OpenLCA Nexus *(66)*. The LCA was conducted for 3D-Molded Wood that was treated by the 15-minute delignification process (as shown in Table S7) and surface coated with 0.05 g PUR/g of 3D-Molded Wood (measured in the lab).

Figs. S25 and S26 show the results of 3D-Molded Wood prepared from 15-min delignification treatment based on the specific tensile strength and the specific stiffness, respectively. Al alloy with high recycled content (73.9%) was chosen for this comparison because of its lower environmental impacts compared with Al alloy with low recycled content, as shown in Table S5. Figs. S25 and S26 shows significant reductions of environmental impacts of 3D-Molded Wood prepared from 15 mins of delignification compared to 3D-Molded Wood made by 48 hours of delignification (42–93% reduction in Fig. S25, 36–93% reduction in Fig. S26). The 3D-Molded Wood prepared from 15 mins of delignification also has lower environmental impacts compared to the high recycled content Al alloy (> 52% lower across all environmental impact categories).

Figs. S27 and S28 show the results of the 3D-Molded Wood uncoated and coated with PUR compared with the Al alloy on the basis of the specific tensile strength and the specific stiffness, respectively. Adding PUR coating increases the environmental impacts of 3D-Molded Wood slightly, but the results are still lower than the environmental impacts of Al alloy with high recycled content.

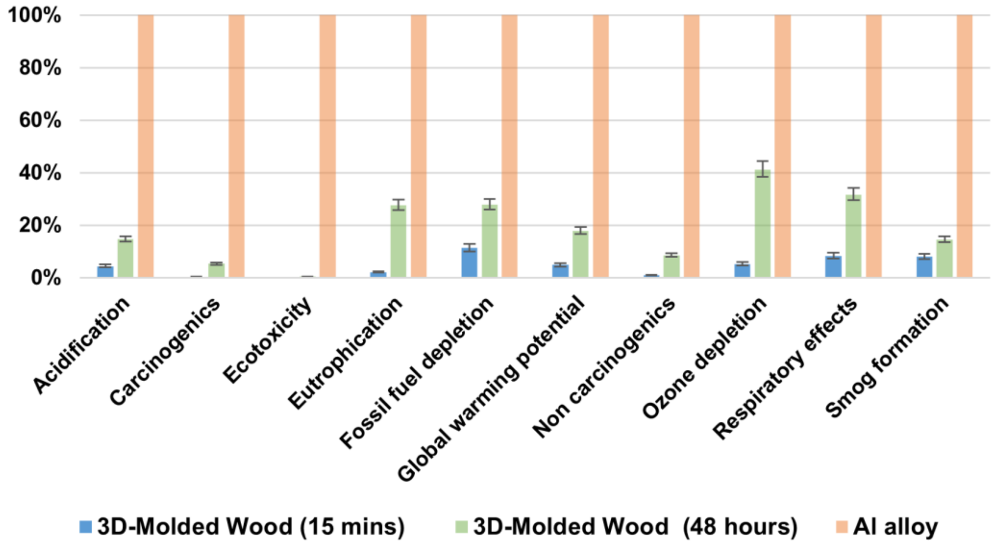

Fig. S25. Environmental impacts per cm^3/MPa based on the specific tensile strength for 3D-Molded Wood prepared from 15-minute delignification treatment shown in **Table S7**, normalized to the higher impact material for each environmental impact category (Al alloy in the high recycling scenario with 73.9% recycled content).

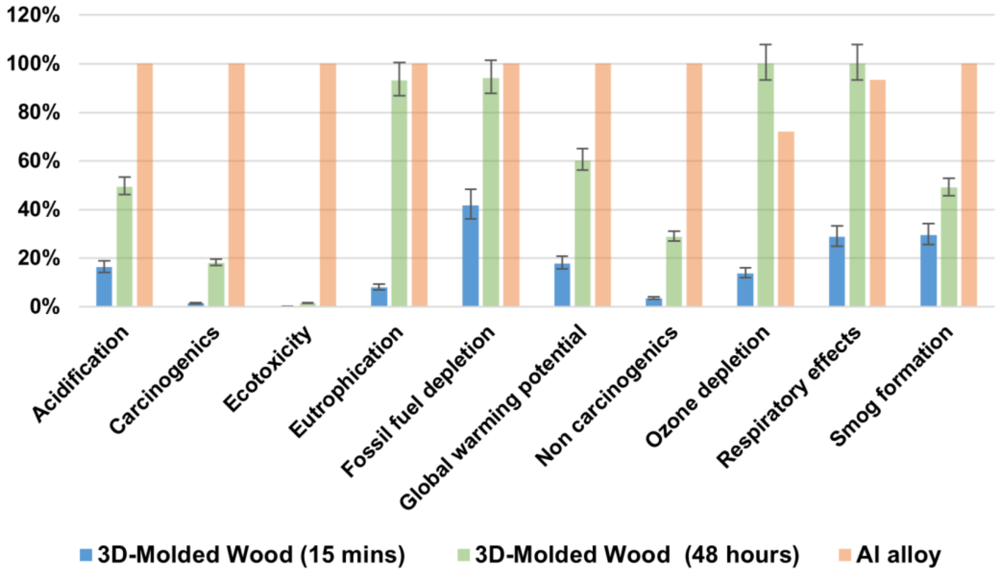

Fig. S26. Environmental impacts per cm^3/GPa based on the specific stiffness for 3D-Molded Wood prepared from 15-minute delignification treatment shown in **Table S7**, normalized to the higher impact material for each environmental impact category (Al alloy in the high recycling scenario with 73.9% recycled content).

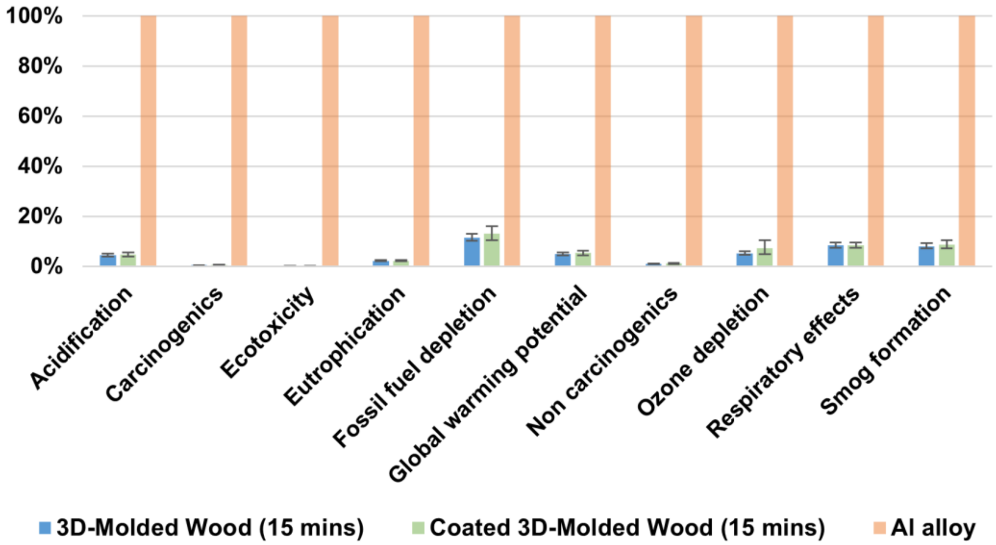

Fig. S27. Environmental impacts per cm^3/MPa based on the specific tensile strength for 3D-Molded Wood prepared from the 15-minute delignification treatment shown in **Table S7** and coated with PUR, normalized to the higher impact material for each environmental impact category (Al alloy in the high recycling scenario with 73.9% recycled content).

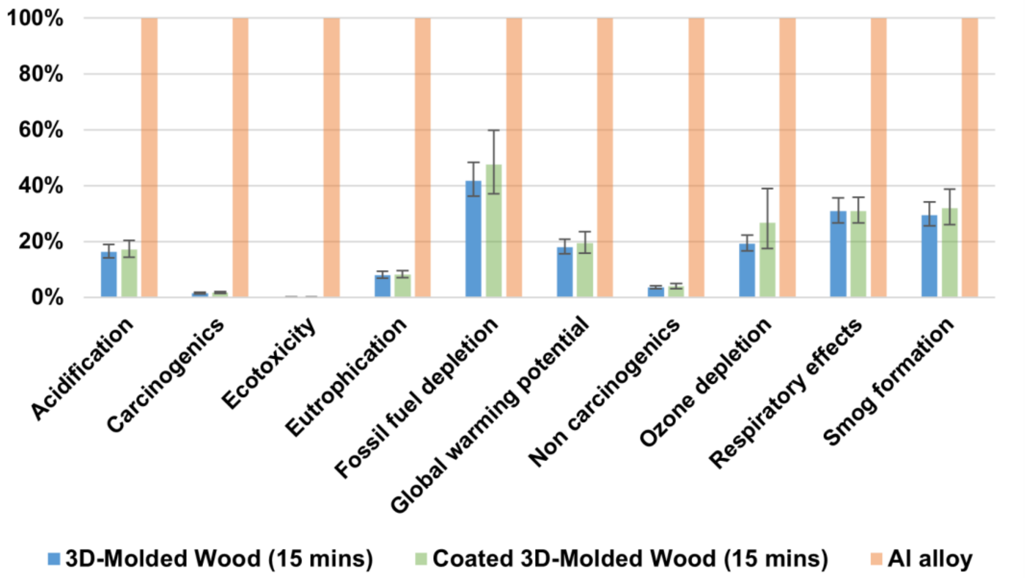

Fig. S28. Environmental impacts per cm^3/GPa based on the specific stiffness for 3D-Molded Wood prepared from the 15-minute delignification treatment shown in **Table S7** and coated with PUR, normalized to the higher impact material for each environmental impact category (Al alloy in the high recycling scenario with 73.9% recycled content).

Fig. S29. Photographs of 3D-Molded Wood made from various species of hardwoods, including balsa, walnut, elm, and paulownia, in which the materials can be (A) folded or (B) molded parallel to the wood fiber direction without any damage, showing excellent foldability.

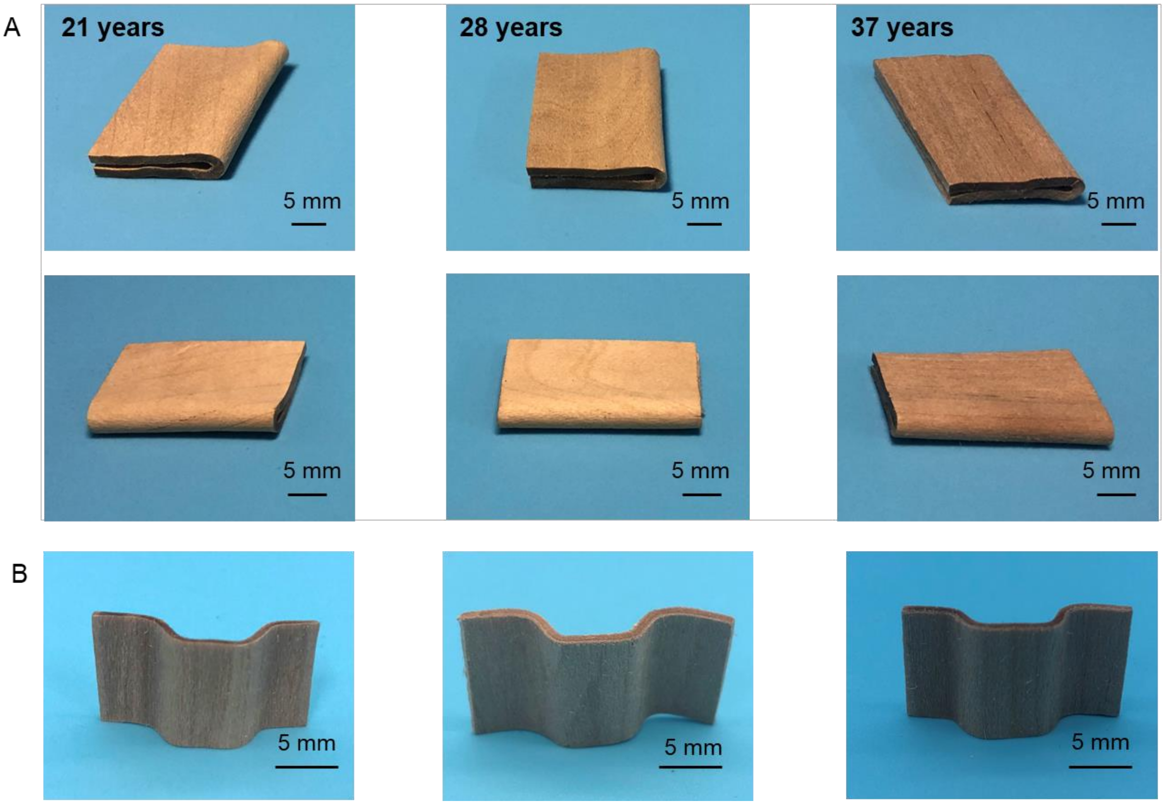

Fig. S30. Photographs of 3D-Molded Wood made from basswood with different ages of tree, in which the materials can be (A) folded or (B) molded parallel to the wood fiber direction without damage.

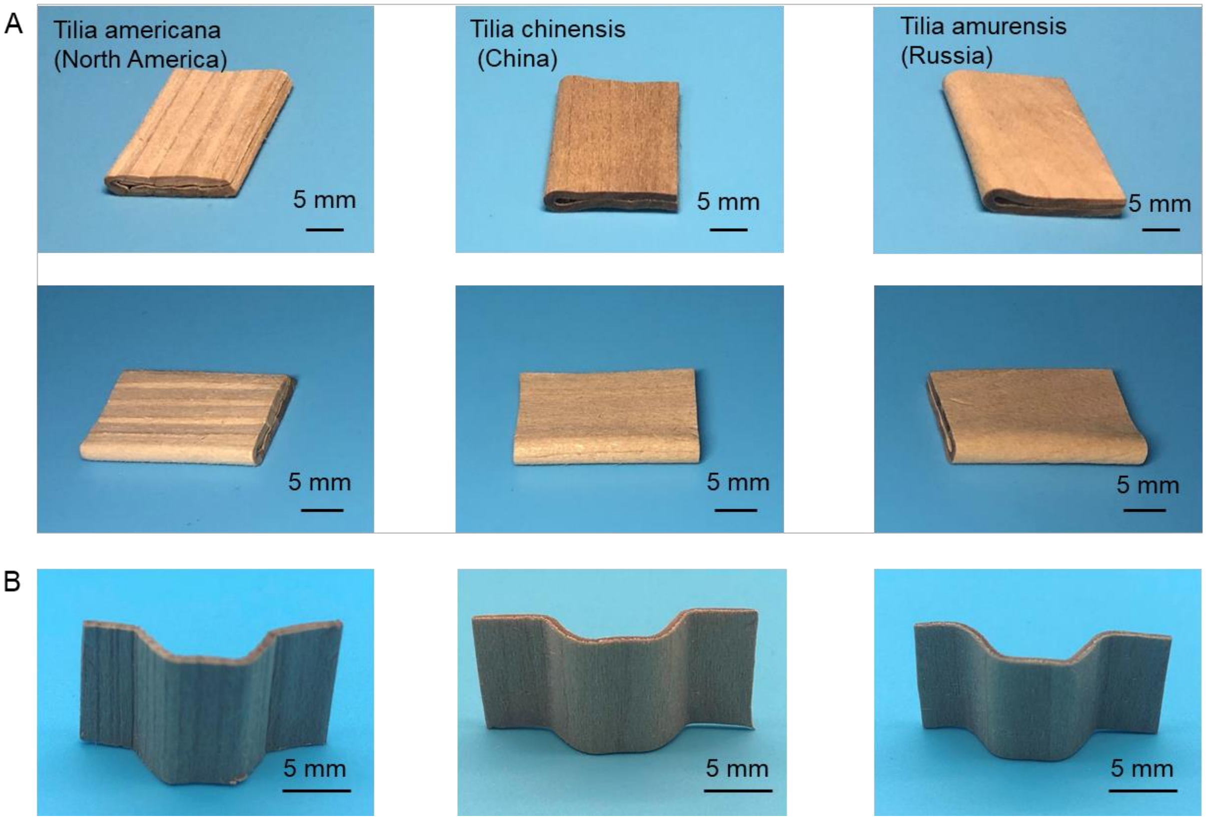

Fig. S31. Photographs of 3D-Molded Wood made from basswood with different environmental exposures/locations, in which the materials can be (A) folded or (B) molded parallel to the wood fiber direction without damage.

Movie S1. The rapid size change process from Shrunken Wood to Moldable Wood.

Movie S2. The high foldability of Moldable Wood.

Movie S3. The “water-shock” process from Shrunken Wood to Moldable Wood.

Movie S4. The rolling and twisting process of Moldable Wood.

References

1. S. Xu *et al.*, Assembly of micro/nanomaterials into complex, three-dimensional architectures by compressive buckling. *Science* **347**, 154-159 (2015).
2. Y. Kim, H. Yuk, R. Zhao, S. A. Chester, X. Zhao, Printing ferromagnetic domains for untethered fast-transforming soft materials. *Nature* **558**, 274-279 (2018).
3. C. Wang, C. Wang, Z. Huang, S. Xu, Materials and structures toward soft electronics. *Adv. Mater.* **30**, 1801368 (2018).
4. Y. Tang *et al.*, Programmable kiri-kirigami metamaterials. *Adv. Mater.* **29**, 1604262 (2017).
5. A. K. Naskar, J. K. Keum, R. G. Boeman, Polymer matrix nanocomposites for automotive structural components. *Nat. Nanotechnol.* **11**, 1026-1030 (2016).
6. A. I. Taub, Automotive materials: technology trends and challenges in the 21st century. *Mrs. Bull.* **31**, 336-343 (2006).
7. K. Zheng, D. J. Politis, L. Wang, J. Lin, A review on forming techniques for manufacturing lightweight complex—shaped aluminium panel components. *Int. J. Lightweight Mater.Manuf.* **1**, 55-80 (2018).
8. X. Liao *et al.*, High strength in combination with high toughness in robust and sustainable polymeric materials. *Science* **366**, 1376-1379 (2019).
9. P. Fratzl, R. Weinkamer, Nature's hierarchical materials. *Prog. Mater. Sci.* **52**, 1263-1334 (2007).
10. Q.-F. Guan *et al.*, Lightweight, tough, and sustainable cellulose nanofiber-derived bulk structural materials with low thermal expansion coefficient. *Sci. Adv.* **6**, eaaz1114 (2020).
11. D. Adam, Aluminium producers promise a cleaner smelting pot (vol 557, pg 280, 2018). *Nature* **558**, 18-18 (2018).
12. C. Chen *et al.*, Structure–property–function relationships of natural and engineered wood. *Nat. Rev. Mater.* **5**, 642-666 (2020).
13. E. Toumpanaki, D. U. Shah, S. J. Eichhorn, Beyond what meets the eye: imaging and imagining wood mechanical–structural properties. *Adv. Mater.* **33**, 2001613 (2021).
14. A. Geng, H. Yang, J. Chen, Y. Hong, Review of carbon storage function of harvested wood products and the potential of wood substitution in greenhouse gas mitigation. *Forest Policy Econ.* **85**, 192-200 (2017).
15. G. Churkina *et al.*, Buildings as a global carbon sink. *Nat. Sustain.* **3**, 269-276 (2020).
16. Y. Pan *et al.*, A large and persistent carbon sink in the world's forests. *Science* **333**, 988-993 (2011).
17. S. Fink, Transparent wood–a new approach in the functional study of wood structure. *Holzforschung* **46,** 403-408 (1992).
18. M. I. Shams, H. Yano, A new method for obtaining high strength phenol formaldehyde resin-impregnated wood composites at low pressing pressure. *J. Trop. For. Sci.* **21**, 175-180 (2009).
19. J. Gierer, Chemistry of delignification. *Wood Science and technology* **19**, 289-312 (1985).
20. R. M. Seborg, M. A. Millett, A. J. Stamm, Heat-stabilized compressed wood (Staypak). (1956).
21. H. Yano, A. Hirose, P. J. Collins, Y. Yazaki, Effects of the removal of matrix substances as a pretreatment in the production of high strength resin impregnated wood based materials. *J. Mater. Sci. Lett.* **20**, 1125-1126 (2001).
22. J. Song *et al.*, Processing bulk natural wood into a high-performance structural material. *Nature* **554**, 224-228 (2018).

23. H. Sivonen, S. L. Maunu, F. Sundholm, S. Jämsä, P. Viitaniemi, Magnetic resonance studies of thermally modified wood. *Holzforschung* **56,** 648-654 (2002).
24. B. F. Tjeerdsma, M. Boonstra, A. Pizzi, P. Tekely, H. Militz, Characterisation of thermally modified wood: molecular reasons for wood performance improvement. *Holz. Roh.Werkst.* **56**, 149-153 (1998).
25. S. Trey, S. Jafarzadeh, M. Johansson, In situ polymerization of polyaniline in wood veneers. *ACS Appl. Mater. Inter.* **4**, 1760-1769 (2012).
26. V. Merk *et al.*, Hybrid wood materials with magnetic anisotropy dictated by the hierarchical cell structure. *ACS Appl. Mater. Inter.* **6**, 9760-9767 (2014).
27. C. Mai, H. Militz, Modification of wood with silicon compounds. Inorganic silicon compounds and sol-gel systems: a review. *Wood. Sci. Technol.* **37**, 339-348 (2004).
28. P. N. Hasluck, Ed., *Manual of Traditional Wood Carving* (Courier Corporation, 1977).
29. M. J. Golden, Ed., *A Laboratory Course in Wood-turning* (Harper & Brothers, 1897).
30. B. Hahn, T.-E. Werner, P. Haller, Experimental and numerical investigations on adhesively bonded tubular connections for moulded wooden tubes. *Constr. Build. Mater.* **229**, 116829 (2019).
31. T. Saito, R. Kuramae, J. Wohlert, L. A. Berglund, A. Isogai, An ultrastrong nanofibrillar biomaterial: the strength of single cellulose nanofibrils revealed via sonication-induced fragmentation. *Biomacromolecules* **14**, 248-253 (2013).
32. A. Walther, J. V. I. Timonen, I. Díez, A. Laukkanen, O. Ikkala, Multifunctional high-performance biofibers based on wet-extrusion of renewable native cellulose nanofibrils. *Adv. Mater.* **23**, 2924-2928 (2011).
33. X. Yang *et al.*, Surface and interface engineering for nanocellulosic advanced materials. *Adv. Mater.* **23**, 2002264 (2021).
34. I. A. Kinloch, J. Suhr, J. Lou, R. J. Young, P. M. Ajayan, Composites with carbon nanotubes and graphene: An outlook. *Science* **362**, 547-553 (2018).
35. C. Chen *et al.*, Highly elastic hydrated cellulosic materials with durable compressibility and tunable conductivity. *ACS Nano* **14**, 16723-16734 (2020).
36. Z. Fang *et al.*, Critical role of degree of polymerization of cellulose in super-strong nanocellulose films. *Matter* **2**, 1000-1014 (2020).
37. A. Dupleix, L. Denaud, L. Bléron, R. Marchal, M. Hughes, The effect of log heating temperature on the peeling process and veneer quality: beech, birch, and spruce case studies. *Eur. J. Wood Wood Prod.* **71**, 163-171 (2013).
38. D. W. Green, J. E. Winandy, D. E. Kretschmann, "Mechanical properties of wood" in *Wood Handbook: Wood as an Engineering Material. Madison, WI: USDA Forest Service, Forest Products Laboratory, 1999. General technical report FPL;(1999) pp. 4.1-4.45*.
39. D. W. A. Rees, Ed., *Mechanics of Optimal Structural Design: Minimum Weight Structures*. (John Wiley & Sons, 2009).
40. T. Bitzer, Ed., *Honeycomb Technology* (Springer Netherlands, 1997).
41. C. Moes, G. Hibbard, Development of melt-stretching technique for manufacturing fully-recyclable thermoplastic honeycombs with tunable cell geometries. *Mater. Design* **141**, 67-80 (2018).
42. M. Peresin *et al.*, Large-scale nanofibrillated cellulose film: an overview on its production, properties, and potential applications. *4th International Conference of Pulping, Papermaking and Biotechnology (ICPPB 2012)*, (2012).

43. B. Netz, O. R. Davidson, P. R. Bosch, R. Dave, L. A. Meyer, *Climate change 2007: Mitigation. Contribution of Working Group III to the Fourth Assessment Report of the Intergovernmental Panel on Climate Change. Summary for Policymakers*. (Intergovernmental Panel on Climate Change (IPCC), Geneva, 2007), pp. 23 pp.

44. X. Luo *et al.*, Evaluation of mountain beetle-infested lodgepole pine for cellulosic ethanol production by sulfite pretreatment to overcome recalcitrance of lignocellulose. *Ind. Eng. Chem. Res.* **49**, 8258-8266 (2010).
45. M. B. Tucker, T. Li, Strain deconcentration in thin films patterned with circular holes. *Int. J. Appl. Mech.* **01**, 557-568 (2009).
46. N. G. Gonzalez-Canche, E. A. Flores-Johnson, P. Cortes, J. G. Carrillo, Evaluation of surface treatments on 5052-H32 Al alloy for enhancing the interfacial adhesion of thermoplastic-based fiber metal laminates. *Int. J. Adhes. Adhes.* **82**, 90-99 (2018).
47. https://www.alibaba.com/product-detail/Caustic-soda-Flakes-99-Sodium-hydroxide_60585020668.html?spm=a2700.themePage.feed.2.344c233dZzpI1e.
48. https://www.alibaba.com/product-detail/Na2so3-Na2so3na2so3na2so3-Sodium-Sulfite-Anhydrous-Technical_1600088309337.html?spm=a2700.galleryofferlist.normal_offer.d_title.7b544749x1wENP&s=p.
49. https://detail.1688.com/offer/522557800822.html?spm=a26352.13672862.offerlist.6.171a5a6bYMmhJ9.
50. https://www.alibaba.com/product-detail/5052-harga-cut-thin-types-of_1600132515331.html?spm=a2700.galleryofferlist.normal_offer.d_title.2f0029aeon0U54.
51. D. Zenkert, The Handbook of Sandwich Construction. *North European engineering and science conference series*, (1997).
52. International Standard Organization, *ISO 14040: Environmental Management - Life Cycle Assessment - Principles and Framework*. (2006).
53. https://www.openlca.org/.
54. K. Kamau-Devers, S. A. Miller, The environmental attributes of wood fiber composites with bio-based or petroleum-based plastics. *Int. J. Life Cycle Assess.* **25**, 1145-1159 (2020).
55. M. F. Ashby, Ed., *Materials and the Environment: Eco-informed Material Choice* (Elsevier Science, 2012).
56. G. Wernet *et al.*, The ecoinvent database version 3 (part I): overview and methodology. *The International Journal of Life Cycle Assessment* **21**, 1218-1230 (2016).
57. PE International AG, "Life cycle assessment of rough-sawn kiln-dried hardwood lumber" (PE International AG for AHEC - American Hardwood Export Council, 2012).
58. J. C. Bare, Tool for the Reduction and Assessment of Chemical and Other Environmental Impacts (TRACI), Version 2.1 - User’s Manual; EPA/600/R-12/554 2012.
59. T. Eggeman, in *Kirk‐Othmer Encyclopedia of Chemical Technology*.
60. Water Main Break Rates In the USA and Canada: A Comprehensive Study. An Asset Management Planning Tool for Water Utilities.
61. US Department of Transportation Commodity Flow Survey Data and Reports. https://www.bts.gov/topics/commodity-flow-survey-reports (accessed 01/23/2020).
62. U.S. Life Cycle Inventory Database. (2012). National Renewable Energy Laboratory, 2012. Accessed 01/15/2021: https://www.lcacommons.gov/nrel/search.

63. Advancing Sustainable Materials Management: 2018 Fact Sheet, EPA, Assessing Trends in Materials Generation and Management in the United States. 2020. Washington, DC.
64. M. Tuomela, M. Vikman, A. Hatakka, M. Itävaara, Biodegradation of lignin in a compost environment: a review. *Bioresour. Technol.* **72**, 169-183 (2000).
65. F. Asina *et al.*, Biodegradation of lignin by fungi, bacteria and laccases. *Bioresour. Technol.* **220**, 414-424 (2016).

66. OpenLCA Nexus. https://nexus.openlca.org/database/OzLCI2019. Accessed 9/10/2021.